Neutron Transmutation Doping of Two-Dimensional Materials.

by

Sushant Sambhaji Lakhavade

A Thesis Presented in Partial Fulfillment
of the Requirements for the Degree
Master of Science

Approved July 2023 by the
Graduate Supervisory Committee:

Sefaattin Tongay, Chair
Terry Alford
Sui Yang

ARIZONA STATE UNIVERSITY

August 2023

ABSTRACT

Doping is the cornerstone of Semiconductor technology, enabling the functionalities of modern digital electronics. Two-dimensional (2D) transition metal dichalcogenides (TMDCs) have tunable direct bandgaps, strong many-body interactions, and promising applications in future quantum information sciences, optoelectronic, spintronic, and valleytronic devices. However, their wafer-scale synthesis and precisely controllable doping are challenging. Moreover, there is no fixed framework to identify the doping concentration, which impedes their process integration for future commercialization. This work utilizes the Neutron Transmutation Doping technique to control the doping uniformly and precisely in TMDCs. Rhenium and Tin dopants are introduced in Tungsten- and Indium-based Chalcogenides, respectively. Fine-tuning over 0.001% doping level is achieved. Precise analytical techniques such as Gamma spectroscopy and Secondary Ion Mass Spectrometry are used to quantify ultra-low doping levels ranging from 0.005-0.01% with minimal error. Dopants in 2D TMDCs often exhibit a broad stokes-shifted emission, with high linewidths, due to extrinsic effects such as substrate disorder and surface adsorbates. A well-defined bound exciton emission induced by Rhenium dopants in monolayer WSe_2 and WS_2 at liquid nitrogen temperatures is reported along with specific annealing regimes to minimize the defects induced in the Neutron Transmutation process. This work demonstrates a framework for Neutron Doping in 2D materials, which can be a scalable process for controlling doping and doping-induced effects in 2D materials.

ACKNOWLEDGEMENTS

Wolfgang Bollich (Ex radiation safety officer, ASU) for his help with getting this project approved. This research would not have been possible without the excellent facilities of the Eyring Materials Center at Arizona State University.

I want to extend my heartfelt appreciation to Dr. Zerrin Uzum for her unwavering support and encouragement throughout this journey. I am incredibly grateful to my roommates and best friends, Brij Khajuria, Ashay Nagdive, and Neeraj Borade. Their friendship and positive energy made my time at ASU enjoyable.

Lastly, I am indebted to my parents, Snehal Lakhavade and Sambhaji Lakhavade who have always believed in me and supported me.

TABLE OF CONTENTS

LIST OF TABLES

LIST OF FIGURES

Figure   Page

Figure 9: Bandgap Variations Due to Strain (Solid Blue Lines Represent the Excitonic Bright and Valence Bands, Respectively; Dashed Gray Lines Represent the Dark Excitonic Band) b. Demonstrates an Illustration of 1L-WSe$_2$ Strained Over a SiO$_2$ Nanopillar (W Atoms in Blue and Se in Yellow). Neutral Excitons, Represented as e−h Pairs, are Created within the Excitation Laser Spot (Red Dashed Line) Funnel to Low-Potential Strained

x

1. INTRODUCTION

1.1 The Advent of 2D Materials

In many ways, developing two-dimensional (2D) materials represents a full circle in materials synthesis, growing atom by atom, layer by layer, reminiscing the earliest moments of the universe, and forming the first elements. Only the so-called precursors existed in the early phases of the universe, formed from the primordial soup of particles that filled the cosmos[1]. These particles were drawn together through Coulombic forces, forming the plasma-enhanced vacuum chambers we call stars[2]. Within the heart of the stars, the fusion of lighter elements gave birth to heavier ones, creating elements like carbon, nitrogen, and oxygen[1].

Although the underlying mechanisms are significantly different, the term nucleation in epitaxial growth of 2D materials is loosely inspired by the nucleation mechanism in stellar nucleosynthesis, a process of creating a stable nucleus that can grow into a larger nucleus by additions of protons and neutrons in stars[1]. However, the heaviest elements in the universe - those beyond iron – required a different process for their formation. Neutron-rich environments of supernovae or neutron star mergers caused heavy neutron irradiation of these elements through "neutron capture." During neutron capture, a nucleus captures a neutron, and the elemental nuclei reach an excited state and quickly decay to the ground state, emitting gamma rays and adding atomic mass by one. These higher mass nuclei beta decay where neutron decays into a proton, followed by electron and anti-neutrino emission. Finally, a new element with an atomic number higher than one from the primary element is formed. This process is called the Nuclear Transmutation of elements. It can repeat several times, eventually creating elements such

1

as gold, platinum, and uranium[3]. The Neutron Transmutation Doping method also relies on this mechanism of neutron capture and will be discussed in detail in chapters 3 and 4.

In 2004, Andre Geim and Constantine Novoselov found a way to isolate graphene layers from graphite. Graphene is a single layer of graphite composed of carbon atoms arranged in a hexagonal lattice with sp^2 hybridization[4]. It has a hexagonal unit cell with a six-fold rotation axis (C^6) and three mirror planes (m), which makes it a P6/mmm space group[5].

Graphene has unique properties due to its layered structure and high surface-to-volume ratio. For example, it has a very high charge carrier mobility, ranging from 2000 to 5000 cm^{-2}/Vs, making it suitable for high-speed FETs operating at terahertz frequencies. Graphene also has a very high optical transparency of up to 98%, a very high thermal conductivity of 5000 W cm^{-1} K^{-1}, a very high Young's modulus of 1 TPa, and an excellent surface area of 2630 m^2g^{-1}.

Graphene's almost zero-band gap could be helpful for many applications, but semiconductors with intermediate and tunable bandgaps are more desirable for the electronics and optoelectronics industry. In this regard, 2D materials TMDs have the potential to have a tunable bandgap and form heterostructures, which makes them attractive for many electronic and optoelectronic applications, including the next generation CMOS devices. From a materials science perspective, the success of the electronics and optoelectronics industry is mainly due to the availability of sizeable low-defect density single crystals of Si, III–V, and II–VI compounds.

1.2 Transition Metal Chalcogenides.

2D Materials have reduced dielectric screening making them more susceptible to external electric fields. These materials exhibit novel physical and chemical properties that differ from their bulk counterparts due to quantum confinement and crystal symmetry effects[6]. Quantum confinement of excitons (electron-hole pairs) is due to the reduction in dimensions of material restricting the electronic wave function and quantizing one dimension[7]. This confinement can result in discrete energy levels and enhanced optical and electronic properties.

Transition metal dichalcogenides (TMDCs) are a class of 2D materials that have the general formula MX_2, where M is a transition metal (such as Mo or W), and X is a chalcogen (such as S or Se). TMDCs have a layered structure, where each layer consists of a hexagonal plane of metal atoms sandwiched between two hexagonal planes of chalcogen atoms. These layers are held together by weak van der Waals forces, which allow for easy exfoliation and stacking of different layers. TMDCs also exhibit quantum confinement and crystal symmetry effects that make them attractive for various applications, such as optoelectronics, catalysis, and spintronics[6].

1.2.1 Tungsten-Based TMDs.

At equilibrium conditions, 2D Transition Metal Dichalcogenides (TMDs) belong to the symmetry D^{3h} group with transition metal and chalcogen atoms arranged in hexagonal symmetry. In their bulk form, these layered materials are bonded together by weak Van der Waals forces. As shown in figure 1, DFT calculations show that Tungsten based TMDs like WS_2 and WSe_2 are semiconducting with an indirect bandgap. Conduction band minima were found between the high symmetry points of Γ and K high, while the valence band maxima were found at the Γ point, indicating an indirect band gap of bulk MX_2.
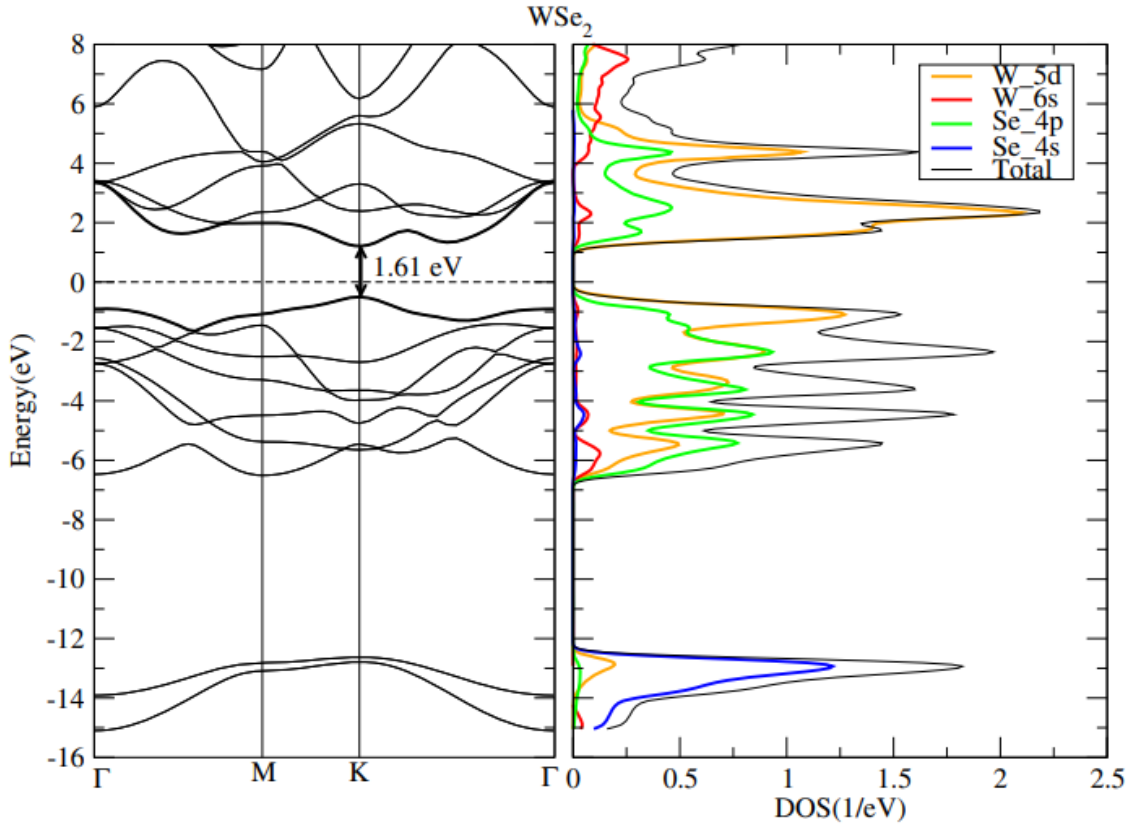
Figure 1: (Color online) Electronic Band Structure and Corresponding Total and Partial Density of States of 1H-WSe$_2$. A Direct Band Gap of 1.71 eV is Shown, Which Occurs at K High Symmetry Point. All the Partial DOS are Multiplied by 1.5. The Fermi Level is Set at 0 eV[8].

At the monolayer level, both the CBM and VBM were found at the K high symmetry point. The calculated band gap of 2H-WSe$_2$ is close to the experimentally-measured optical band gap of 1.80 eV. Notably, the optical band gap of a monolayer is always smaller than the fundamental band gap; the excitonic binding energy compensates for the difference. In the calculated Phonon Density of states (on the right), it is seen that the bands on both the valence and the conduction site originate primarily from the d-orbitals of the transition metals. These d states of metal atoms are hybridized with the s states of chalcogen atoms[8]. Since bands and states around the Fermi energy are mainly derived from d orbitals of Mo

and W, increases in the chalcogens' atomic number (from S to Te) produce wider d bands around the band gap, reducing the band gap[8].

Due to the quantum confinement effect, the electronic properties of the bulk crystal drastically change from their monolayer counterparts, undergoing an indirect to direct bandgap transition in the monolayer limit (Figure 2).
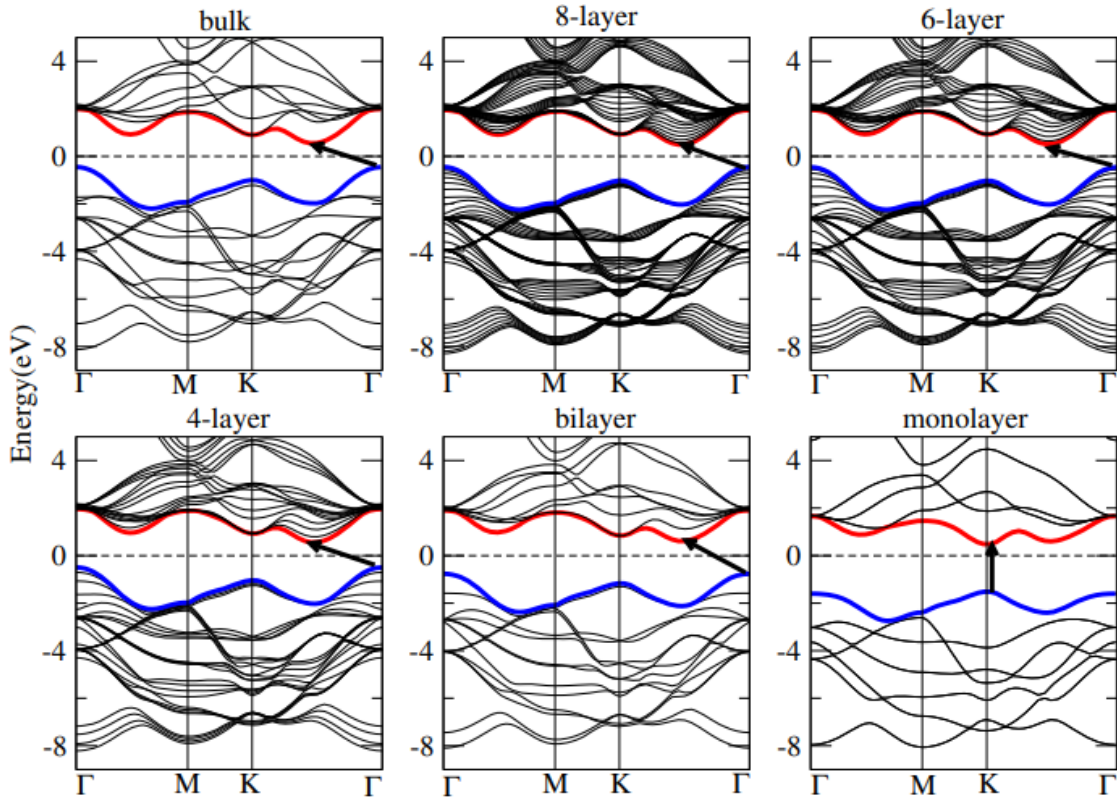
Figure 2: Electronic Band Structure of Bulk WS_2, its Monolayer, and Polylayers. VBM (blue) and CBM (red) are Highlighted. The Arrow Indicates the Direct Band Gap[8].

1.2.2   Excitons in TMD Semiconductors

TMDs offer a unique platform to study the rich physics of excitons. Due to the weak dielectric screening and strong geometrical confinement, the Coulomb interaction is powerful, leading to various excitonic phenomena, such as different excitons. These excitons have binding energies of about 0.5 eV at room temperature, much larger than

those in conventional materials, such as Si, GaAs[9,10]. Therefore, excitons are stable at room temperature and determine these materials' optical properties and non-equilibrium dynamics. This excitonic contribution increases radiative recombination at room temperature, causing high-intensity photoluminescence (Fig 3a). Moreover, higher-order excitonic quasiparticles, such as trions (e-e-h or e-h-h charged excitons)[11,12] and biexcitons (XX)[13] have been detected in monolayer TMDs.

The field of TMD optics and optoelectronics witnessed a surge of interest in 2010 when Heinz[14] and Wang[15] demonstrated that Molybdenum disulfide (MoS_2) changes from an indirect-gap semiconductor in the bulk form to a direct-gap material in monolayer MoS_2 (figure 3b). This results in a significant enhancement of PL (figure 3a). By using first-principle calculations and tight binding models to analyze the orbital character of the electronic states at the relevant high-symmetry points (K and K), it was shown that the observed transition could be explained as a result of a momentum/orbital selective interlayer splitting of the primary relevant energy levels.[16]
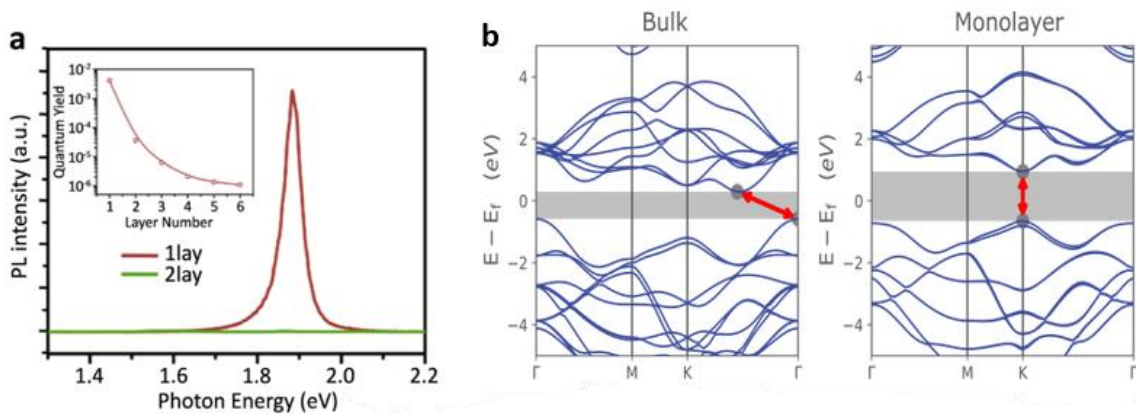
Figure 3: a Drastically Enhanced Layer-Dependent PL Intensity for MoS_2 Monolayers Confirming the Transition to a Direct-Gap Semiconductor[14] **b** Indirect to Direct Bandgap Transition from Bulk to Monolayer MoS_2. Adapted from ref. [16]

The optical properties of TMDs are characterized by two strong resonances denoted as A and B excitons[14]. They originate due to reduced dielectric screening and spin-orbit coupling, which gets stronger with increasing atomic numbers due to higher interacting orbitals. Heavy transition materials lift the spin degeneracy of the valence and the conduction band since electrons of different spins have different energies. The spin-orbit coupling splits the energy levels of the electrons and holes in TMDs as per their spins, creating two sub-bands for each valence and conduction band. This means that each band is divided into two parts, one for electrons with spin up and one for electrons with spin down. While the splitting is relatively tiny for the conduction band, the valance band separation reaches approximately 200 meV in molybdenum-based and even 400 meV in tungsten-based TMDs[17]. As a result, two optical transitions are possible, involving holes in the upper and lower energy spin valence bands. The effect of the spin-orbit coupling is more significant for the valence band than the conduction band because the valence band electrons are closer to the nucleus and experience a stronger electric field. The effect is also more significant for tungsten-based TMDs than molybdenum-based TMDs because tungsten has a higher atomic number than molybdenum and, thus, a stronger electric field.[17]

1.2.3 Exciton Linewidths

The low-temperature measurement provides valuable information about the excitonic transitions in monolayer WSe_2 on a sapphire substrate. The radiative lifetime of these transitions was determined to be approximately 200 fs, corresponding to a linewidth of 3 meV.[18] In contrast, when hexagonal boron nitride (hBN) is used to encapsulate the samples, narrower linewidths as small as 1.7 meV have been observed.[19]
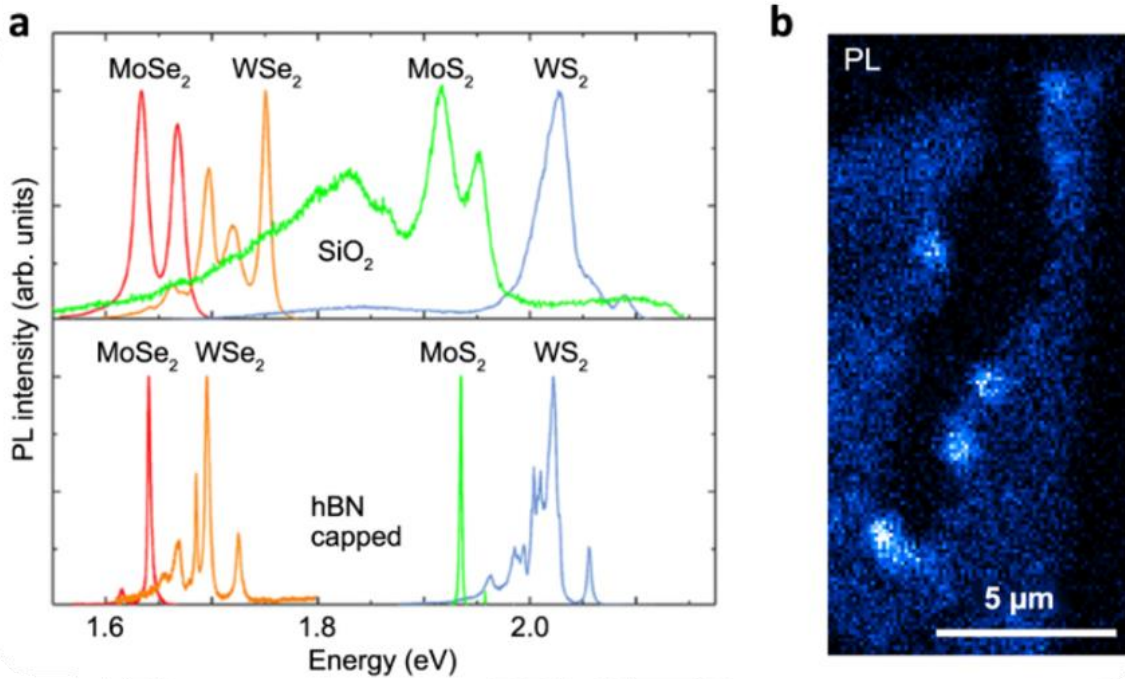
Figure 4: PL Spectra for Different TMD Monolayers at 4 K Illustrating a Series of Resonances at Low Energies that can be Ascribed to Localized Excitonic States (top). hBN-Encapsulated TMDs Show Narrow Linewidths (Bottom)[19]. **b** PL Images of a WSe$_2$ Monolayer Scratched with a Needle Illustrating Pronounced Light Emission from Edges (Courtesy of R. Bratschitsch, Univ. Münster).

Additionally, it was observed that the excitonic linewidth exhibited a linear increase with temperature up to 50 K. This increase was attributed to non-radiative scattering processes that occur when excitons interact with phonons, which are quantized vibrations of the crystal lattice. In the case of weak excitation, exciton-phonon scattering is the main mechanism responsible for the scattering. The linear relationship between the excitonic linewidth and temperature is a characteristic signature of acoustic phonons. This is because, at low temperatures, the distribution of acoustic phonons follows the Bose-Einstein distribution, which scales linearly with temperature[20]. As the temperature rises above 100 K, optical phonons play a more significant role in the scattering processes, leading to a super-linear temperature dependence. This dependence produces a broader

linewidth of approximately 30-40 meV at room temperature. Optical phonons are associated with vibrations involving the lattice atoms' displacements and are more energetic than acoustic phonons.[20]
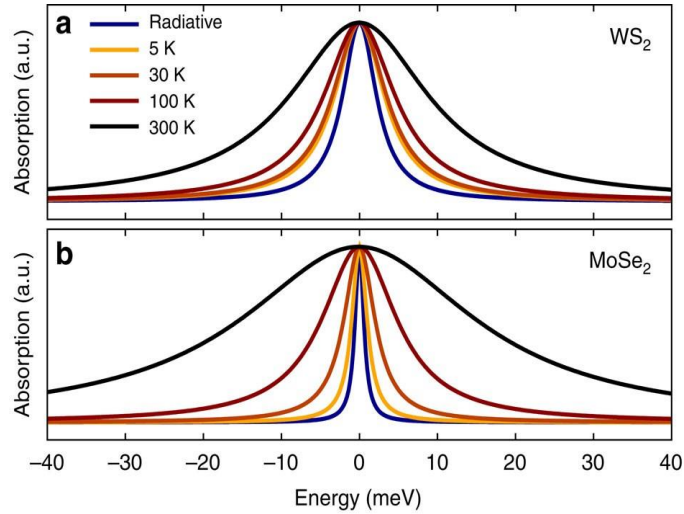
Figure 5: Predicted Temperature-Dependent Absorbance Spectra of **a** WS_2 **b** $MoSe_2$.

Scattering behavior differs between molybdenum-based transition metal dichalcogenides (TMDs) and tungsten-based TMDs. For molybdenum-based TMDs, scattering within the same energy valley (around the K valley) is predicted to be crucial. On the other hand, for tungsten-based TMDs, scattering into energetically lower dark excitons becomes the dominant scattering channel. Dark excitons refer to excitonic states that do not directly emit light and have lower energies compared to bright excitons[20]

1.2.4 Exciton Dynamics and Photoluminescence

Extensive theoretical and experimental investigations have been conducted to explore the fundamental processes that govern the behavior of excitons, encompassing optical excitation, exciton formation, exciton thermalization, and exciton decay.

At first, TMDs are stimulated by incident light, generating coherent excitons known as excitonic polarization. In low excitation-level scenarios, these coherent excitons decay through two primary mechanisms: radiative coupling, emitting light, and exciton-phonon scattering, involving their interaction with lattice vibrations or phonons[21]. Within a period typically less than a picosecond, efficient phonon-assisted processes facilitate the conversion of excitonic polarization into a population of incoherent excitons[21].
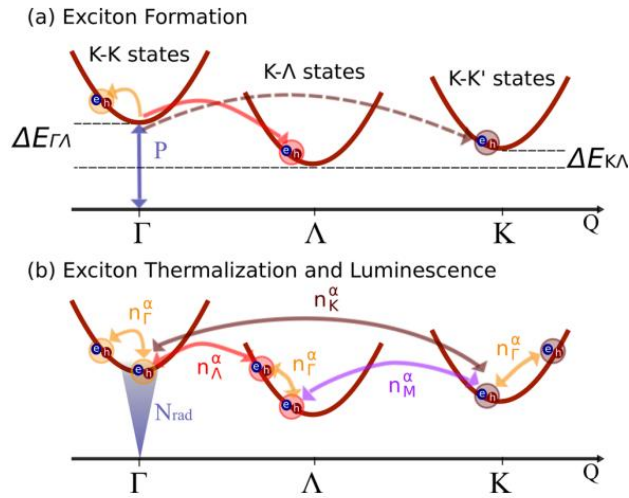
Figure 6: Exciton Dynamics **a** Formation, and **b** Thermalization and Luminescence.

Following this initial stage, exciton thermalization ensues, driven by the emission and absorption of both acoustic and optical phonons. This process encompasses a cascade of transitions, deexciting the excitons from higher to lower energy states. The journey includes traversing a series of bright and dark excitonic states that resemble the familiar Rydberg series. Eventually, the excitons reach the ground state, resulting in the

establishment of a thermalized exciton distribution.[22] In scenarios where the excitation intensity is medium to strong, exciton-exciton scattering assumes significance. This intriguing phenomenon involves interactions between excitons, with Auger scattering playing a prominent role. Auger scattering facilitates the rapid annihilation of excitons through non-radiative processes, diverting them from radiative recombination[22].

1.2.5   Localized Excitons

It is impossible to grow 100% pure monolayers, and TMDs often contain impurities or experience strain, leading to the formation of localized excitons as electrons and holes become trapped in potential wells. At room temperature, the photoluminescence (PL) spectra of TMDs primarily exhibit a broad peak corresponding to the bright 1s exciton transitions (figure 4 b). However, at lower temperatures, additional narrow resonances become visible below the bright 1s excitons, as depicted in (figure 4 b). These resonances arise from free excitons that are trapped within localized potential wells. The presence of these resonances diminishes as the temperature increases, as thermal energy becomes sufficient to overcome the trapping potential.[23]

1.3 Defects in 2D Materials

The second law of thermodynamics states that if a system is in thermal equilibrium concerning its surroundings, there will always be a degree of disorder, which makes defects in crystalline solids inevitable. From a crystal growth perspective, the number of defects or impurities when synthesized near equilibrium conditions is always lower than those grown at conditions far from equilibrium due to higher disorder or entropy. Defects also appear due to pressure, oxidation, or bombardment from energetic particles. Defects

strongly influence the electronic, optical, magnetic, and thermal properties hence controlling defects or doping is the cornerstone of modern electronics and the advent of semiconductors. The word "Defect" mostly has a negative connotation. Still, in semiconductors, especially 2D materials, they make exotic phenomena possible, like color centers in wide bandgap semiconductors[24], pinning of magnetic vortices on defects in type-2 superconductors[25], formation of flat bands where doped carriers enable the construction of a two-dimensional plasmon[26].

In recent years, irradiation-induced defects have been studied widely since they can create localized doping effects and tailor material properties. These studies are also helpful in developing advanced semiconductors for space applications and those inside a fusion/fission reactor, owing to their importance in space applications. In 2D layered materials, defect formation energy is very high, and defect concentration over a wide range of temperatures is negligible. However, defects can also arise due to surface interactions, making controlled doping in 2D challenging .[27]

1.3.1 Point Defects in 2D TMDCs

Point defects, such as missing or additional atoms, can significantly influence semiconductors' transport and optical characteristics by trapping electrons, holes, and excitons. When excitons are captured by defects and recombined, they emit light at lower energies than direct optical transitions. This effect is more pronounced in lower dimensions where electron wavefunction confinement is stronger than bulk. Shallow defects in three-dimensional semiconductors have binding energy determined by the mass and dielectric constant. However, the dimensionality effect increases the binding energy in two-dimensional semiconductors. This shift in binding energy and recombination

dynamics has essential implications for excitons in two-dimensional materials, indicating more excellent stability and emission properties at elevated temperatures.[28]

Anion, vacancy-generated point defects, were created after energetic alpha particle irradiation, and their concentration could be controlled by modulating the irradiation dose in monolayer WSe_2 and $MoSe_2$. These defects induce a new emission peak at 0.15 to 0.25 eV below the free-exciton PL peak, and its intensity is enhanced as the defect density increases. Furthermore, the overall PL intensity also increases at higher defect densities, and thus, the defective material becomes more luminescent compared to pristine monolayers[29].
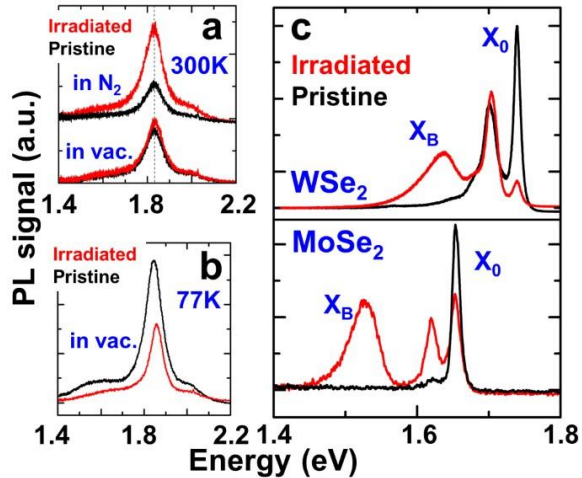
Figure 7. a Room Temperature PL Spectrum of MoS_2 in the Presence of N_2 or Vacuum Before and After Irradiation (Dose ~ 8×10^{13} cm^{-2}). **b** PL Spectra at 77 K in a Vacuum. **c** PL Spectra were Taken at 77 K in N_2 on WSe_2 and $MoSe_2$ Monolayers Before and After the Irradiation. Adapted from ref [29]

It is important to note that bound exciton (X_B)was only observed in the presence of nitrogen. The authors modeled the band structure and density of states in the presence of di-sulfur vacancies and concluded that the gas molecules drain free electrons via the anion defect site causing an excitonic transition from charge to a neutral state. [29]

1.3.2 Transition Metal Doping in 2D TMDCs

In the past few years, various methods have been developed to advance doping in 2D materials, such as adsorption of organic molecules[30], electrostatic doping[31], substitutional doping[32], and plasma doping[33]. Substitutional doping is an energetically favorable and desirable technique where substituting atoms replace metal or chalcogen atoms in the host lattice and form covalent bonds with the neighboring atoms. Prominent studies include CVT doping in bulk crystals of MoS_2 and WSe_2 with Nb, Re, or V, which were grown by chemical vapor transport and then mechanically exfoliated into thin flakes. This technique has limited control over doping due to uncontrollable variation in crystal stoichiometry. Other types of undesired defects such as vacancies and interstitials also form which degrade the overall efficiency More recently, substitutional doping of monolayer TMDCs was achieved by in situ methods such as powder vaporization and gas-source chemical vapor deposition. The optical and transport properties of these monolayer films can be tuned by changing the doping concentration, and they are stable in air [34]. However, controlling the doping concentration and understanding the uniformity of dopant distribution over large areas are still challenging issues.

1.3.3 Dopant Formation Energies

Forming a defect in a perfect crystal is always an energy-intensive process. Otherwise, defects would appear in the crystal even at zero temperature, meaning the crystal would have a different lowest energy configuration. The energy needed to make a defect in the perfect material is called defect formation energy. E_f, is always positive. For a point defect in a single-element solid, an atom substitutes another atom's position in the crystal lattice. The defect formation energy can be calculated as follows:

$$E_f = E_{tot}[\text{point}] - E_{tot}[0] + \mu_{\text{host}} \qquad (1)$$

The total energy of the system (at T = 0) with a point defect is E_{tot}[point] and without a point defect is E_{tot}[0]. The chemical potential of the atom in the perfect system is μ_{host}. For simplicity, it is assumed here that the defect has no charge; that is, there is no extra charge on the defect. This is usually true in metallic systems but not always in semiconductors and insulators.[35] Substitution doping with transition metals can effectively control the Fermi Level with minimum compensation from intrinsic defects[36] Heavy metals like Nb, Ta, and Re are an obvious choice for substitutional doping in Tungsten based TMDs as they are neighbors of Tungsten in the periodic table. Nb and Ta act as p-type dopants. Nb_W and Ta_W have the lowest formation energies and shallow acceptor levels, which can lead to a high level of p-type doping. In comparison, the most critical n-type dopants, Re_W, have relatively higher formation and more profound ionization energies, which can lead to n-type doping, but with lower free electron density. N-type doping is most effective by Re doping under the Se-rich condition[36].

1.3.4   Rhenium Doping in Tungsten based TMDs
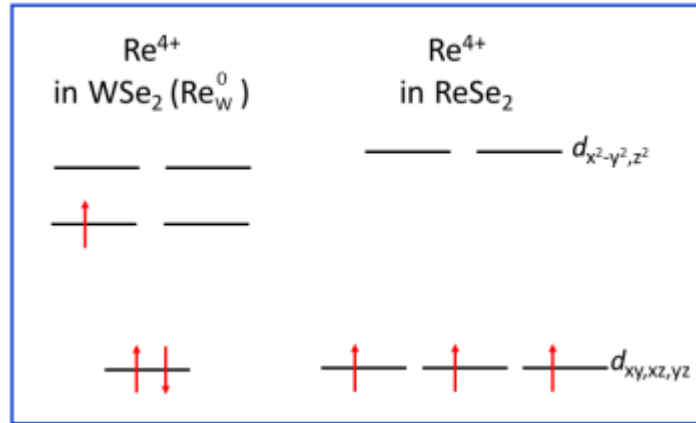
Figure 8: Schematic of Crystal Field Splitting and Electron Filling for Re4+ in WSe$_2$ and its Respective Secondary Phase ReSe$_2$

Rhenium, an electron donor in Tungsten-based Chalcogenides, is the closest neighbor of Tungsten. The relatively deep states of ReW are due to a Re-induced bound state below the CBM, which is produced primarily by the d-d coupling between the Re dopant and the adjacent W ions. On the other hand, $ReSe_2$ has a $P\bar{1}$ crystal structure [37] [figure 8)] $Re4+$ (a d3 ion) has a distorted octahedral environment in which the three d electrons of $Re4+$ occupy the low-lying nonbonding dxy , dxz, and dyz orbitals in the majority spin channel. When a Re atom with a +4 oxidation state substitutes a $W4+$ ion in WSe_2, one of the three d electrons is forced into the higher energy $d_{x^2-y^2,xy}$ orbital. This gap in energy $Re4+$ from $ReSe_2$ to WSe_2 has to be overcome with relatively high energy, resulting in a higher formation energy of Re_W in WSe_2. Hence Rhenium doping is challenging in monolayer TMDCs. Notably, stable dopants in TMDs show higher relaxation times and can produce localized emissions. These emissions are also responsible for fascinating applications such as Single Photon Emission in 2D TMDCs at lower temperatures,

1.4 Single Photon Emission

Single-photon emitters (SPEs) are essential for many quantum photonic applications[38], such as quantum communication, cryptography, metrology, and linear optical quantum computing. However, conventional semiconducting single-photon sources such as InAs, and quantum dots face challenges due to limited scalability and growth[39]. Two-dimensional (2D) materials like hexagonal boron nitride and transition metal dichalcogenides (TMDs) like $MoSe_2$ and WSe_2[40] have shown single photon emissions previously. Monolayer WSe_2 has several advantages over conventional III–V semiconducting quantum dots, such as high-photon interactions and scalability, which

makes it an attractive candidate[40] for future Single Photon sources. Very sharp emissions at low temperatures characterize these sources.

Reports indicate that SPEs in WSe_2 may be caused by localized defect-bound excitons in K-K' valley. This becomes possible form when the energy of the dark excitonic band of WSe_2 is lowered and hybridizes with a valley symmetry-breaking defect state at strained regions (figure 9 b), as mentioned in the previous section on Rhenium doping[41] (figure 9 a). Strain and defects are crucial for the creation of SPE.

Defects in 2D TMDs are uneven and not easily controllable. Several methods of creating defects like Chalcogen vacancies[42], electron irradiation[43], and diazonium chemistry[44] have been reported. Figure 9 c shows ultra-sharp emissions from defect bands. Higher intensities were observed at higher defect concentrations. This emission is confirmed by measuring second-order correlation, the probability of detecting two photons simultaneously (figure 9 d). Ideally, this correlation function must be zero for pure SPE. Various studies have reported values of 0.05-0.1 for this function.
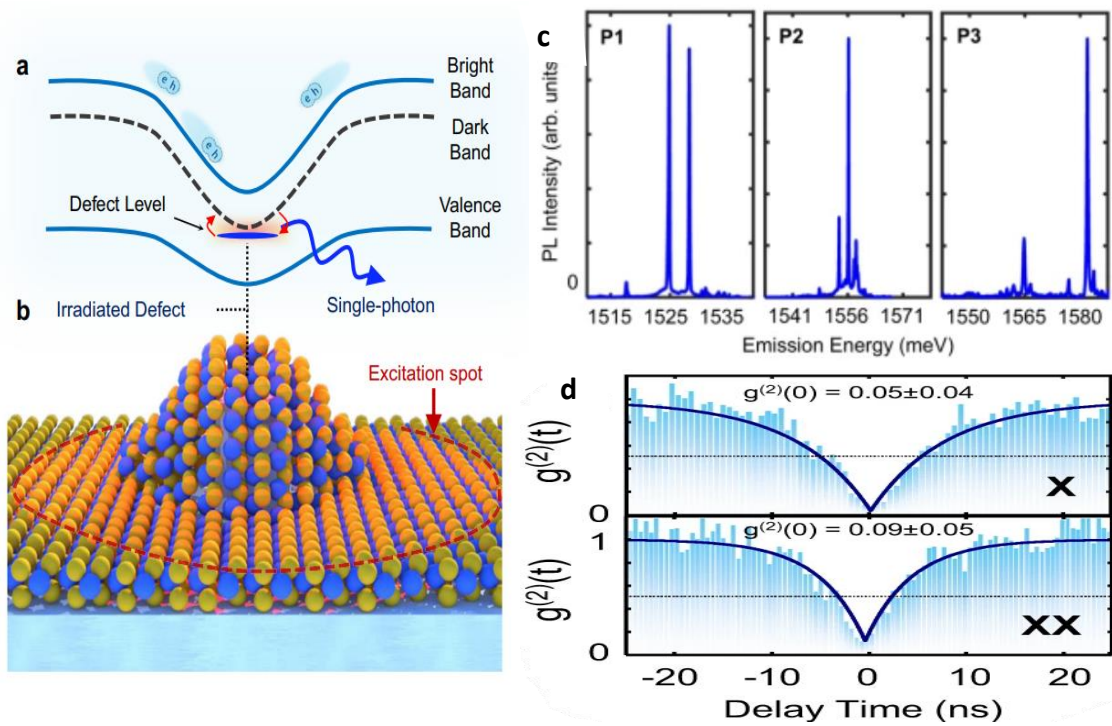
Figure 9: Bandgap Variations Due to Strain (Solid Blue Lines Represent the Excitonic Bright and Valence Bands, Respectively; Dashed Gray Lines Represent the Dark Excitonic Band) **b.** Demonstrates an Illustration of 1L-WSe$_2$ Strained Over a SiO$_2$ Nanopillar (W Atoms in Blue and Se in Yellow). Neutral Excitons, Represented as e−h Pairs, are Created within the Excitation Laser Spot (Red Dashed Line) Funnel to Low-Potential Strained Regions. **c** PL Spectra Demonstrating SPE at Low Temperatures. **d** Second-Order Correlation Measurement [43]

1.4.1 Challenges and Doping Outlook in 2D

One of the most critical challenges for doping in 2D is control over doping concentration and consistency. Like traditional semiconductor research, no universal standard exists to identify the doping concentration in 2D materials. Thus, a standard that includes materials and electrical characterization techniques to fully deconvolute how much doping is required to tune transport properties, understand how the substrate induces some strain, and increase or decrease the doping effects.

The involvement of chemicals also affects the doping/carrier concentration. Finally, due to quantum confinement in 2D, the activation rate of the dopant also

increases. Hence, it is important to understand dopant activation energies in 2D materials and the impact of thermal processes on dopant activation. One final challenge in 2D materials is the experimental realization of theoretical models.

The doping of 2D semiconductors is critical to developing next-generation electronic and optoelectronic devices that leverage the properties of 2D materials.

2. SYNTHESIS AND CHARACTERIZATION

Two-dimensional (2D) materials have a thickness of one or a few atoms or molecules. They exhibit novel physical and chemical properties that differ from their bulk counterparts, such as high surface-to-volume ratio, tunable band gap, and enhanced mechanical strength. Synthesis of 2D materials is crucial for exploring their fundamental properties and potential applications. There are two main approaches for synthesizing 2D materials: top-down and bottom-up. Top-down techniques involve exfoliating or cleavage of bulk-layered materials into thin flakes or sheets, such as mechanical exfoliation, liquid exfoliation, or intercalation exfoliation. Bottom-up approaches involve assembling or growing 2D materials from atomic or molecular precursors, such as chemical vapor deposition (CVD), molecular beam epitaxy (MBE), or self-assembly. Both top-down and bottom-up techniques have advantages and disadvantages regarding the scalability, quality, uniformity, and controllability of 2D materials.

2.1 Top-Down Approach

Top-down methods for synthesizing 2D materials are based on breaking down bulk-layered materials into thin layers or flakes. Various crystal growth techniques can be used for this purpose. These can be classified as follows:

1. Gas-Solid processes (Chemical Vapor Transport)
2. Liquid-Solid Processes (Bridgman Growth, Flux Growth)
3. Solid-Solid Processes (Geometric confinement, Non-epitaxial growth[45]).

2.1.1 Chemical Vapor Transport

The characteristic feature of Chemical Vapor Transport Reactions is that a solid phase, which has a low vapor pressure by itself, can be vaporized with the help of a gas phase reactant, called the transport agent, and then crystallize at another location, usually in the form of crystals. The transport agent can be a halogen, a metal halide, or another compound or mixture that can form a volatile complex with the solid phase. The crystallization occurs when the chemical equilibrium conditions are different at the deposition place than at the vaporization site. Usually, this is achieved by applying different temperatures for vaporization and crystallization, creating a temperature gradient in the system. The temperature gradient also drives the gas flow from the source to the substrate. The chemical equilibrium conditions depend on the partial pressures and the temperature of the gaseous species involved in the reaction [46].

A CVT reaction involves three steps:

- **Step 1**: Sublimation, where the solid source and the mineralizer react to form a gas (Equation (1))

- **Step 2**: Transport, where the gas moves from a high-temperature zone (T1) to a low-temperature site (T2) due to a pressure difference

- **Step 3**: Deposition, where the gas turns back into solid products and releases the mineralizer

The reaction process thermodynamically follows Le Chatelier's principle[47]. This reaction can be expressed as:

$$source_{solid} + mineralizer_{solid} \rightleftharpoons source_{gas} \cdot mineralizer_{gas} \quad (1)$$
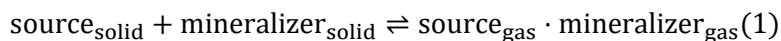
where source$_{solid}$ and mineralizer$_{solid}$ are the solid phases of the source material and the transport agent, respectively, and source$_{gas}$ · mineralizer$_{gas}$ does their reaction in the gas phase form the volatile complex.
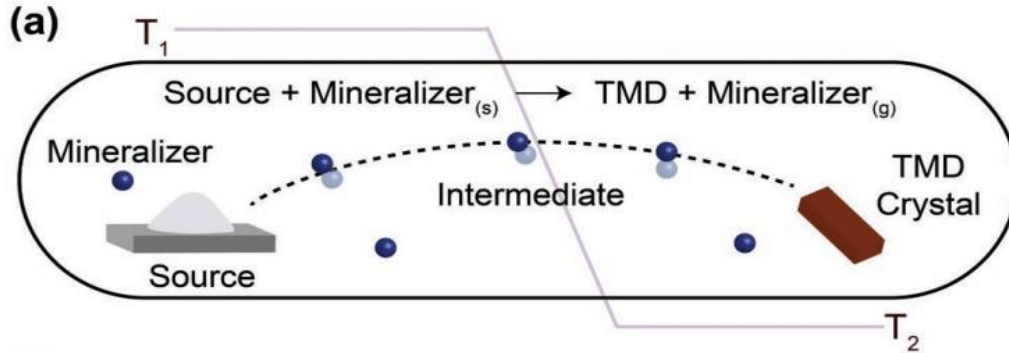
Figure 10: Schematic Showing the Synthesis of Bulk Transition Metal Dichalcogenides (TMDs) by CVT in a Closed System. The Source Materials are Mixed with a Mineralizer, Which Assists the Source Materials' Sublimation at the Enclosure's Hot End (with a Temperature of T$_1$) and the Crystallization Toward the Cold Side (with a Temperature of T$_2$).

In the first step, the solid source reacts with the sublimed mineralizer. It forms a gaseous intermediate in the sublimation zone under a temperature of T$_1$, creating a partial pressure gradient of the gaseous intermediate (forward reaction in Equation (1)). The gaseous intermediate then moves to another region, called the deposition zone, with a temperature of T$_2$ because of the partial pressure gradient. In the next step, the gaseous intermediate converts to deposit products (backward reaction in Equation (1)) and releases mineralizer molecules. The released mineralizer molecules increase the partial pressure of the mineralizer at the deposition zone, and thus they can return to the sublimation zone for further reaction. This way, source materials are transformed into desired products with a small amount of mineralizer. According to the reaction process, proper selection of source materials and mineralizer is essential for a successful CVT reaction.

A vital feature of an ideal CVT reaction is that the response shows good reversibility, neither reactant-favored nor product-favored, at a specific temperature range, meaning the response's equilibrium constant should be close to one[48]. Such good reversibility can allow easy tuning of the reaction direction by slight temperature variations and ensure maximum transport of the gaseous components.

2.1.2   CVT Growth of Bulk TMDs

The crystal growth of TMDs using CVT is an endothermic process due to a positive enthalpy change where sublimation temperature T_1 is set higher than T_2. Due to this control over temperature and vapor pressures, a wide range of TMDs can be grown using CVT. The precursors could be amorphous TMD formed by a direct reaction between the transition metal and chalcogens or in pure elemental form, as shown in figure 10 a. This makes CVT a versatile technique that gives more choice to choose a variety of precursors depending on the applications. Regarding transport agents or mineralizers, the most common choices are halogens (Cl_2, Br_2, I_2) due to their ability to provide a thermodynamic driving force that facilitates both the chemical reaction and the transport process of the transition metal atoms. The transition metal atoms react with the halogen molecules at high temperatures, forming volatile complexes with lower chemical potentials that can be readily transported in the vapor phase. The transition metal atoms dissociate from the halogen molecules at low temperatures, increasing their chemical potentials and forming TMD crystals.

Halogens also exhibit high reactivity and can adapt to different polymorphs or phases of TMDs by varying the temperature and halogen ratio. Considering the safety aspects of Br_2 or Cl_2, halogen-rich compounds such as HCl, $NHBr_4$, or Chalcogen Halide are used[49]. Chalcogen Halides, such as $TeCl_4$, $SeCl_4$, and $TeBr_4$, can also serve as a halogen

source since they decompose at high temperatures and release the transport species if the growth operating temperature is very high. The transport agent amount influences the transport rate and, consequently, the growth kinetics. Generally, a reasonable amount of transport agent is between 5 and 10 mg/cm^3. However, using a large transport agent may pose a safety risk due to overpressure inside the tube at high temperatures. The ideal gas law (PV= nRT) can be used to estimate the vapor pressure within the growth ampoule.

Interestingly, the features of the resulting bulk TMD crystals can be tuned by modulating the precursors and the transport agents, which are the key factors in the CVT-based synthesis of TMD crystals. For instance, in the case of semiconducting WSe_2, different mineralizers such as Br_2, $SeCl_4$, or $TeCl_4$ can induce n-type doping, while I_2 can induce p-type doping[50,51]. This happens because the transport agent can introduce dopants or defects into the TMDs by interacting with their atoms during the CVT growth. In WSe_2, Br_2, $SeCl_4$, or $TeCl_4$ can act as electron donors and create n-type doping by substituting Se atoms or creating Se vacancies, while I_2 can act as an electron acceptor and create p-type doping.

Undoped WSe_2 crystals were grown using CVT. Tungsten and Selenium elemental powder (99.9999% pure from Sigma-Aldrich) were sealed in a quartz ampoule in a 1:2 stoichiometric ratio (along with I_2, which acts as a transport agent). The sealed ampoule was heated in a three-zone furnace for six days, with the precursors kept at 1000 ^{o}C and the crystals grown at 950 ^{o}C.

2.1.3   Synthesis of WS_2

Since the chalcogen evaporation (100−300 °C) temperature is significantly lower than the synthesis and vaporization temperatures of the metal oxides, two independent heaters and temperatures are applied. WO_3 is heated farther from the substrate at

temperatures of 800–1070 °C. WS$_2$ is grown under an inert atmosphere due to the higher reactivity of S in reducing the metal oxide.

$$2WO_{3(s)} + 7S_{(s)} \rightarrow 2WS_{2(s)} + 3SO_{2(g)}$$
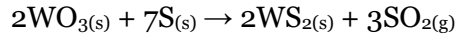
2.1.4   Bridgman Growth

Bridgman Growth is a simple and effective method invented by Percy Bridgman and Donald Stockbarger in 1925. It works by slowly cooling a melted material from hot to cold zones. The desired crystal starts to form at one end of the furnace, where a small crystal is placed to guide the growth. The crystal continues to grow along the length of the furnace until all of the precursors solidify [52]. It works on the same principle of crystallization, where new atoms or molecules are added to the seed cluster (formed by nucleation). The crystal growth rate and quality depend on the number of additional atoms/molecules than the equilibrium concentration at a given temperature, also known as the degree of supersaturation [53].
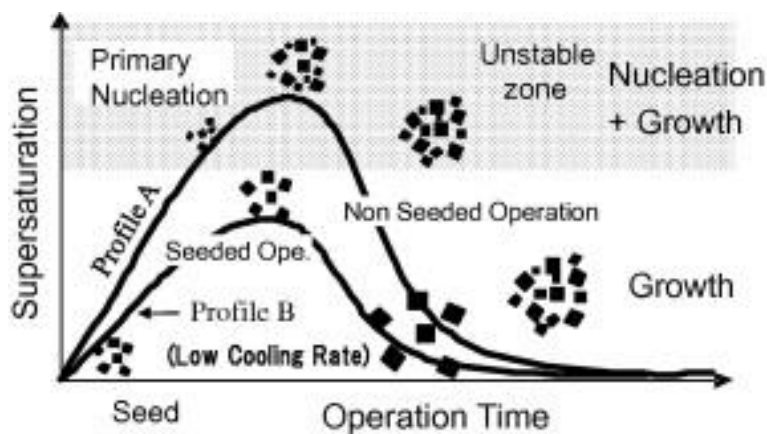
Figure 11: Concentration Profile of a Melt During Crystallization.

25

As shown in figure 11, a high supersaturation caused by a large temperature gradient and growth rate creates a strong driving force for nucleation and growth but also increases the chances of forming defects and impurities in the crystals. For a pure and ideal crystal with minor defects, the Bridgman technique can select a low to moderate growth rate and temperature gradient, which enables pure and high-quality crystal growth[50]. The temperature gradient in Bridgman is still larger than that of the CVT technique, as the former depends on physical transport and diffusion, whereas the latter depends on the chemical transport of the volatile complex.

Bridgman growth is ideal for many materials, provided they do not decompose or undergo phase change before melting. Bridgman ampoules (shown in figure 12) are designed such that one end is pointed to have a single nucleation point. Ampoule cleaning is done by rinsing in soap water, sonication for 10mins, and finally rinsing with de-ionized water. This also makes sure there is no nucleation happening around contaminants. A thermodynamic phase diagram is usually referred to before starting any growth to obtain the temperature and composition at a particular pressure in their equilibrium phase. Phase diagrams are Temperature (T) vs. Equilibrium Concentration (x) plots (figure 12) with vertical separations indicating regions where a particular phase is stable. Sometimes, two phases can also coexist in equilibrium.
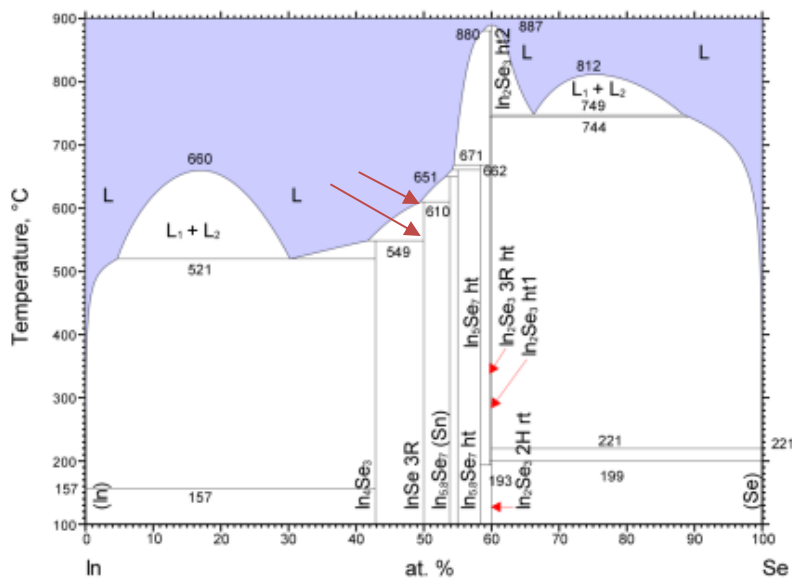
Figure 12: Concentration Profile of a Melt During Crystallization.

2.1.4.1   Growth of Two Different In-Se Phases Used for Transmutation Doping

The InSe 3R phase can be traced with the vertical line at 50 atomic percent at two intersection points, A and B, which give melting points at 549 ºC and 610 ºC, respectively. Elemental powders of Indium and Selenium (99.9999% purity obtained from Sigma-Aldrich) are weighed as per their corresponding stoichiometric ratios. In_2Se_3 phase was also prepared for doping with NTD. For this synthesis, elemental indium and selenium powders were loaded into a quartz ampoule with a pointed tip in a 2:3 stoichiometric ratio. The ampoule was then evacuated to an approximate pressure of 10^{-5} mtorr and sealed. The sealed ampoule was heated at 500 ºC for 24 hours to pre-react the precursors and form polycrystalline In_2Se_3 powder. Recrystallization of the polycrystalline powder was then carried out in the same ampoule. The temperature of the Bridgman furnace was increased to 800 ºC with a temperature gradient of 15 ºC per centimeter, and the ampoule was lowered through the furnace at a rate of 0.5 mm per hour. This step lasted 8 hours and was followed by an additional 8 hours of cooling to bring the furnace to room temperature.
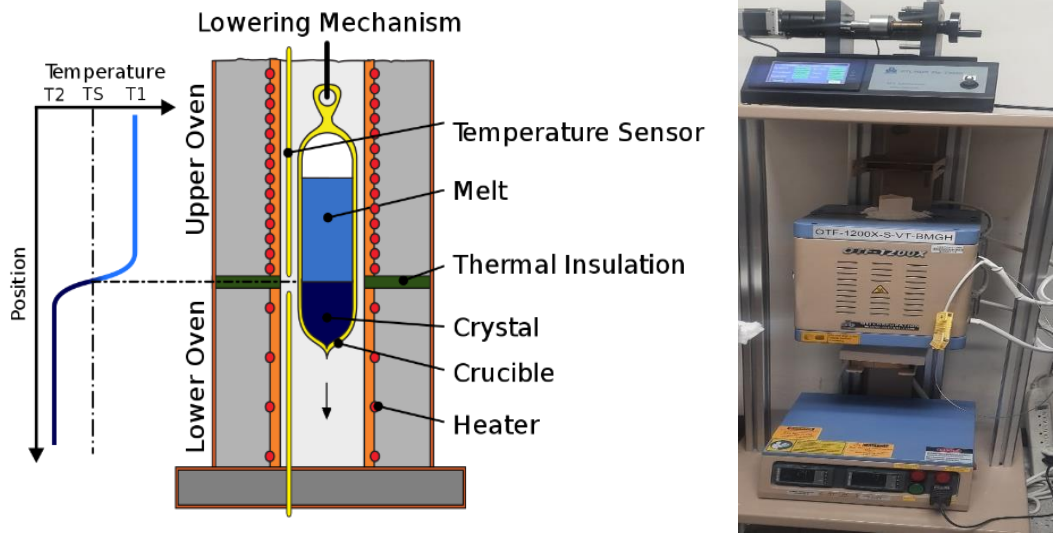
Figure 13: Bridgman Growth Setup **a** Schematic **b** Actual Setup.

2.1.4.2 Setup

Coming to the construction of the Bridgman furnace has two heating zones whose temperature can be controlled and programmed using a PID controller and a lowering device to lower the ampoule through the temperature gradient. The growth starts with the ampoule in the hotter part of the furnace so that it is fully molten (T>Tm). As the tip of the ampoule moves toward the temperature gradient, nucleation starts when it enters the region where T<=Tm [54]. The growth front then moves into the melt as the stable domains develop. Controllable development requires a clearly defined temperature gradient. Even a few grains can form a boule, with many grains formed in parallel because the crystal growth moves in the direction of the temperature differential [54]. For Vdw materials, it is usually easy to extract individual crystals by cleaving with a blade. Many quasi-2D materials have been grown using the Bridgman technique.

2.1.5 Mechanical Exfoliation

Mechanical exfoliation is the most commonly used method to thin down bulk crystals to mono 2D vdW crystals down to a few layers, even monolayer limit, since the successful isolation of graphene monolayer. This is done with the help of Poly Dimethyl Siloxane (PDMS) accompanied by vacuum desiccation for a brief period. Weak Van de Waals interaction between layers made it possible to cleave a relatively large area of thin 2D materials from bulk crystals and attach them to designated substrates.
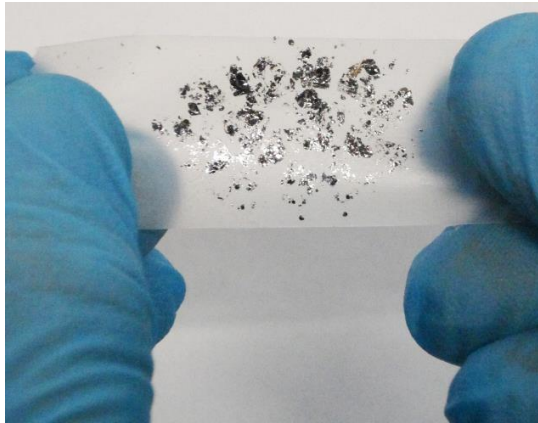
Figure 14: Mechanical Exfoliation of WSe_2 with Scotch Tape.

2.2 Chemical Vapor Deposition (Bottom-Up)

A chemical vapor deposition (CVD) system incorporates temperature regulation, like a continuous variable transmission (CVT), and a pressure and mass flow controller. The system comprises a furnace with single or dual heating zones, with a quartz tube supported. The tube is connected to a gas line at both ends, through which a carrier gas is continuously circulated. Depending on the specific synthesis, the carrier gas can serve as a transportation medium for the reaction precursors and a reducing agent. Unlike CVT, the growth process in CVD is predominantly driven by kinetic factors, in contrast to the sole reliance on precursor thermodynamics.
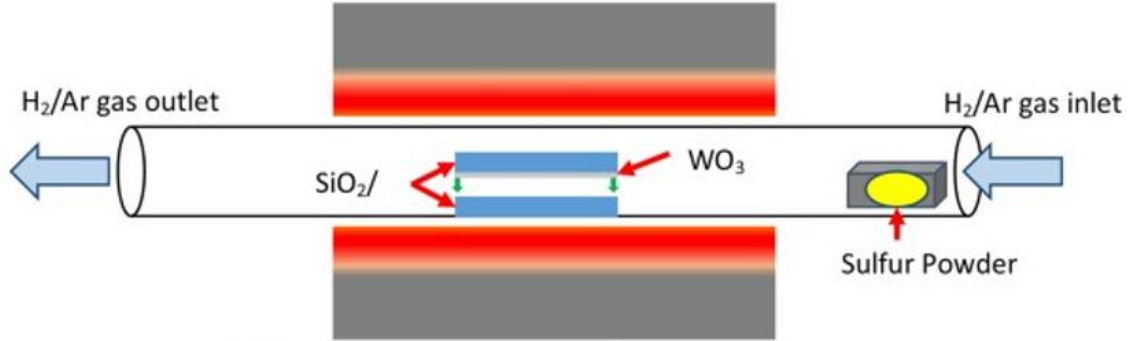
Figure 15: Schematic of a Simple CVD Setup for WS_2 Monolayer Growth.

CVD is a versatile technique for depositing or coating various materials, although the synthesis of group IV and group V materials is not well-developed. In typical CVD setups, precursors in a sublimed state are directed over the desired substrate, such as Si/SiO_2 or Al_2O_3, inside a reaction tube. This is achieved by utilizing an inert carrier gas like Ar or N_2. The chemical reaction occurs on the substrate's surface, which is positioned within a heated region, resulting in the deposition of a thin-film or monolayer on the substrate. Simultaneously, byproducts are removed from the reaction chamber through a pump. Since many CVD processes involve toxic precursors, a reliable purification system is essential to release byproducts into the atmosphere through the purge line safely. A typical CVD schematic is displayed in figure 15. CVD can be performed at varying pressure levels, ranging from millitorr to atmospheric pressure, which can be controlled by a capacitance manometer connected to the downstream side of the chamber.
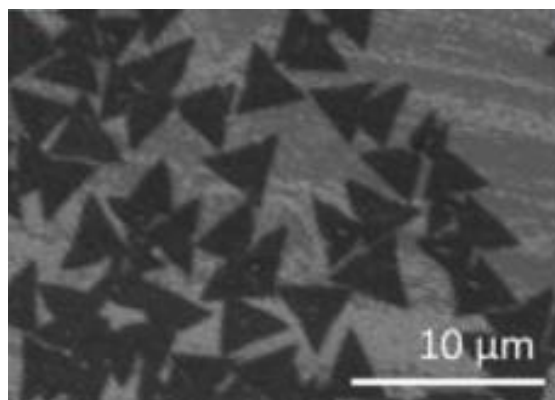
Figure 16: CVD Grown WS_2 Monolayer (H_2 Flow Rate 50 sccm), Scale Bar: 10 μm.

CVD reactions are not limited to the stoichiometry of the reactive precursors, flowrate of the process gas, rate of cooling, wettability of the substrate, and effects of fluid flow along with the boundary layer of the substrate. Another crucial aspect of CVD is sample preparation, which will affect these films' growth quality and crystallinity. Adequate sample preparation can make the substrate more favorable for nucleation, which eventually grows into a more massive lateral-size film over the substrate. The wettability of the substrate surface is often increased by removing any oxide layer deposited on the surface; additionally, nucleating agents such as perylene might be employed to promote growth. Sapphire or SiO_2/Si substrates are generally favored because of their high surface energy.

2.2.1   CVD Synthesis of Tungsten Based TMDs

The synthesis of monolayer WSe_2 was achieved via the AP-CVD method. 60 mg of WO3 precursor was placed in a ceramic boat at the center of the single-zone tube furnace. Double-side polished sapphire substrates were placed on the ceramic boat. Selenium powder was placed upstream in a ceramic crucible in excess, where the temperature was maintained at 250 °C. High purity Ar (≥99.99%) and H_2 gas were passed at 36 sccm and

four sccm flow rates during the entire growth process. The furnace was ramped up with a rate of 30 °C/min to 850 °C and held at 850 °C for 20 minutes before natural cooling to room temperature.

The synthesis of monolayer WS_2 was achieved via the AP-CVD method. 50 mg of WO3 precursor was placed in a ceramic boat at the center of the single-zone tube furnace. Double-side polished sapphire substrates were placed on the ceramic boat. The sulfur powder was placed upstream in a ceramic crucible in excess, where the temperature was maintained at 250 °C. High purity Ar (≥99.99%) and H_2 gas were passed at 50 sccm and 1.5 sccm flow rates during the entire growth process. The furnace was ramped up with a rate of 15 °C/min to 870 °C and gradually cooled to 760 °C in 40 minutes before natural cooling to room temperature.

2.3   Characterization Techniques

This chapter will discuss the principle of characterization techniques used in this work. Based on this, the sensitivity and effectiveness of these techniques are decided.

2.3.1   Secondary Ion Mass Spectroscopy (SIMS)

The secondary Ion Mass Spectroscopy (SIMS) technique can be helpful for the sensitive, quantitative detection of low levels of dopants in semiconductors. A clean and flat sample is bombarded with primary ions ($I_p^{\pm}$), which slowly sputter the sample's surface which can be detected by a secondary ion ($I_s^{\pm}$). When the ion beam energy is low, it enables extremely slow sputtering, and the analysis can be performed by consuming less than a monolayer material. This is called Static SIMS. However, in-depth profiling needs further penetration, so Dynamic SIMS is required for accurate quantitative analysis.
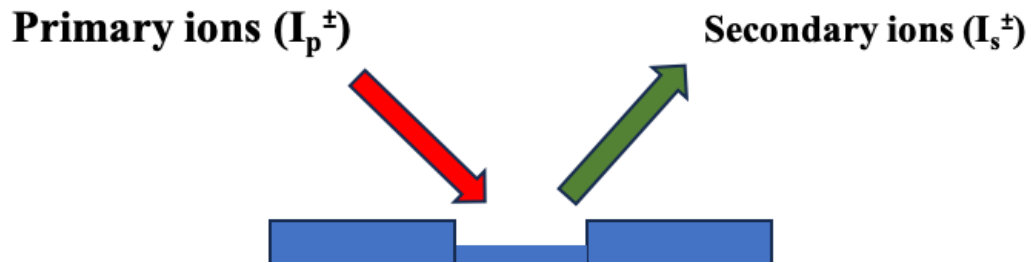
Figure 17: General Working Principle of SIMS.

2.3.1.1 SIMS Primary Ion Sources

Typical SIMS instruments use a duoplasmatron (O- or O_2+) or a surface ionization primary ion source (Cs+). The type of primary ion beam affects the secondary ionization efficiency by changing the chemical and physical properties of the sample surface. Oxygen bombardment creates metal-oxygen bonds in an oxygen-rich zone on the surface. When these bonds break during the sputtering process, the oxygen atoms tend to capture electrons and become negatively charged, while the metal atoms tend to lose electrons and become positively charged. This increases the secondary ionization efficiency for positive ions. Hence a duoplasmatron primary source is more suitable for detecting heavy metals. The duoplasmatron mechanism can be extended to several other gases, but oxygen is the preferred choice as it enhances the ionization efficiency of the surface of positive elements.
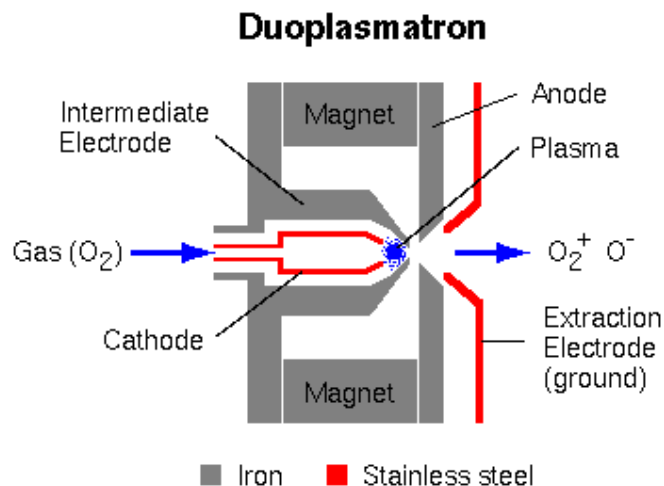
Figure 18: Duoplasmatron Source (Adapted from EAG Labs).

Another type of primary ion source is a Cs+ source. Cesium bombardment lowers the work function of the sample surface, which is the energy needed to remove an electron from the surface. This makes it easier for electrons to escape from the surface and leave behind positive ions, increasing the secondary ionization efficiency for negative ions. Cesium bombardment also increases the amount of cesium on the surface, which can react with other elements and form a negative ion layer.[55] Hence Cs^{+} source is preferable for negative ion formation in electronegative elements.

2.3.1.2 Isotope Ratio Measurements

In measuring Neutron Transmutation Doped samples, the mass resolution should be much higher because the dopant atom has one atomic number higher than the metal in TMD, it has many overlapping isotopes which are chemically similar, have nearly equal ionization, and detector efficiencies do not change much for different isotopes. Our dopant concentrations are much lower than 0.1%, the expected precisions in such measurements.
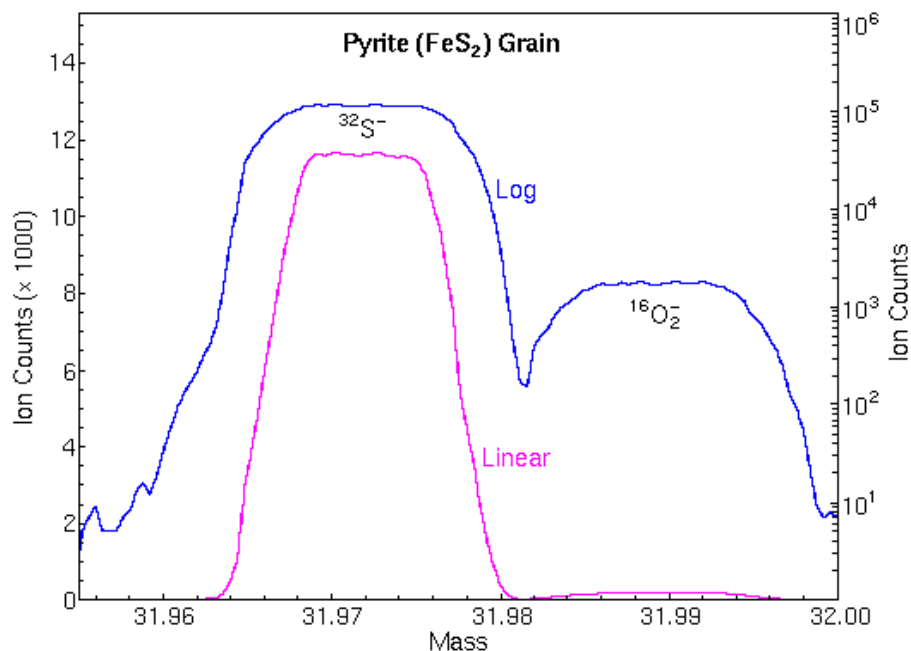
Figure 19: Sulfur Isotope Detection Using SIMS (Adapted from EAG Labs).

Hence further accuracies are necessary, requiring SIMS to be carefully calibrated and any possible interference is eliminated. The isotopic peaks should have flat tops and steep sides so that small changes in the magnet do not affect the amount of ions we measure. Figure 19 represents the typical shape of isotopic peaks and high mass resolution separating O_2 ions from S ions at m/z 32. Both are necessary for measuring accurate 34S/32S isotope ratios. The ratio of isotope amounts must be corrected for minor differences in detector efficiency and slight variations that depend on intensity.

2.3.2   Raman Spectroscopy

Raman spectroscopy is a spectroscopic technique utilized to analyze vibrational, rotational, and other low-frequency modes of materials. It offers comprehensive insights into defect concentration, phase and morphology, crystallinity, and molecular interactions by exploiting the interaction between light and phonons within the crystal lattice[56].

35

In Raman spectroscopy, a monochromatic light source, typically a laser operating in the visible, near-infrared, or near-ultraviolet range, is employed to excite phonons in the crystal lattice, leading to a change in the energy of the photons. This energy shift provides valuable information about the vibrational modes present in the system. The technique involves inelastic light scattering, where incident photons excite the sample, causing the molecule to briefly enter a virtual energy state before emitting the photon. In this process, the energy of the emitted photon is either lower or higher than that of the incident photon, resulting in inelastic scattering. To ensure the total energy of the crystal lattice remains constant after transitioning to a new virtual energy state, the scattered photon changes energy and, consequently, a change in frequency. This energy difference corresponds to the difference between the initial and final states of the lattice. If the final state has higher energy than the initial state, the scattered photon experiences a shift to a lower frequency, known as a Stokes shift or downshift. Conversely, if the final state has lower energy, the scattered photon shifts to a higher frequency, termed an anti-Stokes shift or upshift[56].

Raman shifts are typically expressed in wavenumbers, representing inverse length units, as this value is directly related to energy. The Raman shift (Δv) can be calculated using the equation:
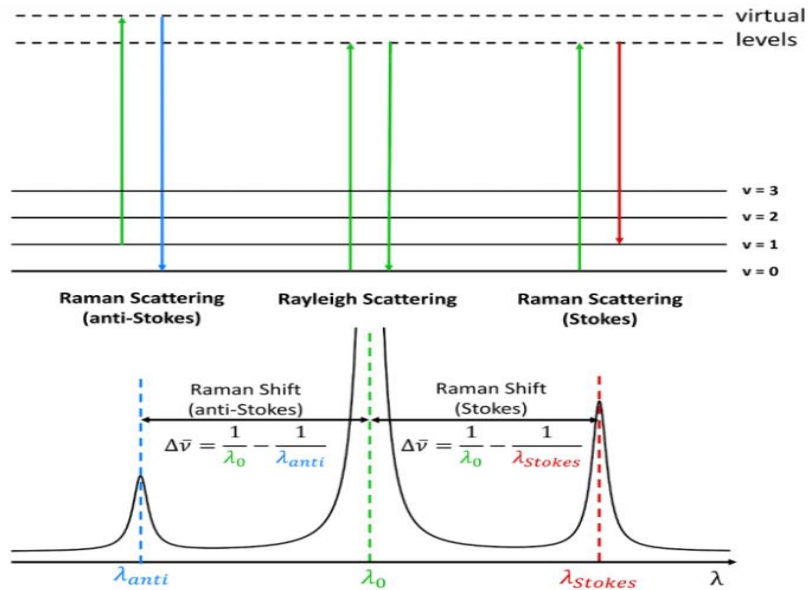
Figure 20: Types of Raman Scattering and Shifts (Adapted from EAG Labs).

$$\Delta\vartheta = \left(\frac{1}{\lambda} - \frac{1}{\lambda^1}\right)$$

Where Δv is the Raman shift expressed in wavelength, λ is the excitation wavelength, and λ^1 is the Raman spectrum wavelength[56].

The basic configuration of a Raman spectrometer comprises essential components such as a laser light source, a charge-coupled device (CCD) detector, and an edge filter. In the provided diagram, the monochromatic laser beam generated by the laser source enters the system through the laser pinhole at the bottom right corner. Subsequently, the laser passes through a sequence of mirrors and filters before reaching the sample, which is focused by a microscope objective. The scattered light originating from the crystal lattice retraces the same optical path and is captured by the photodetector. Concurrently, the Rayleigh rejection filters effectively eliminate the elastically scattered light, commonly known as Rayleigh scattering[56].
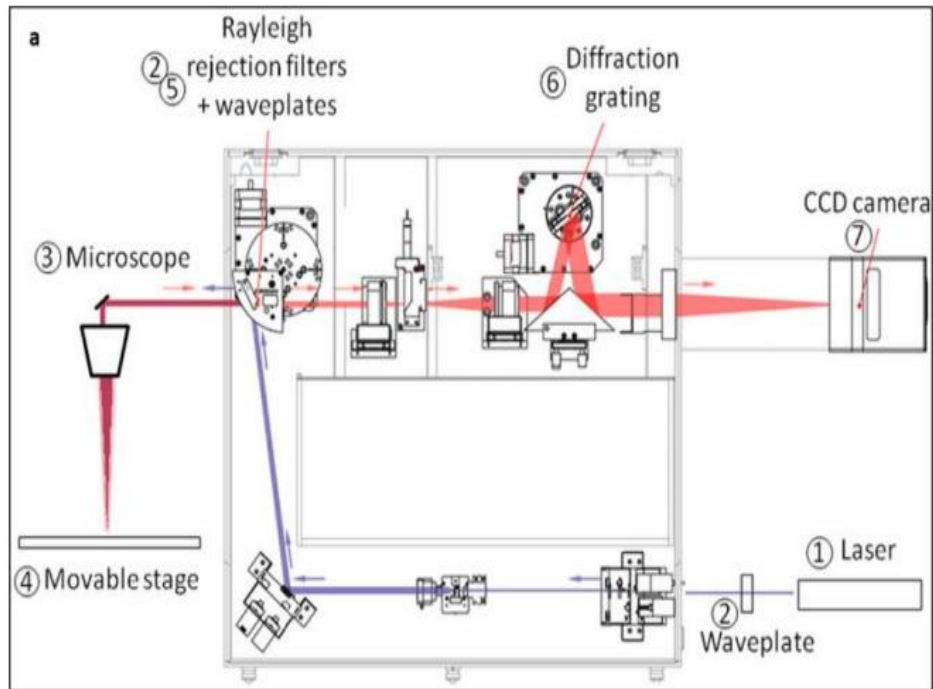
Figure 21: Schematic Representation of Raman Spectrometer © Renishaw.

2.3.3 Photoluminescence Spectroscopy

Photoluminescence spectroscopy (PL) is a non-destructive technique used for material characterization. Photoluminescence refers to the emission of light by matter following the absorption of photons. It can be considered the radiative counterpart to the absorption process. During emission, an electron (or potentially a quasi-particle) residing in a higher-energy state undergoes a discrete transition to an unoccupied lower-energy state (figure 22). In radiative transitions, the energy difference between these two states is released as electromagnetic radiation in the form of photons. On the other hand, non-radiative transitions release this energy difference as heat, specifically in the form of phonons [57].
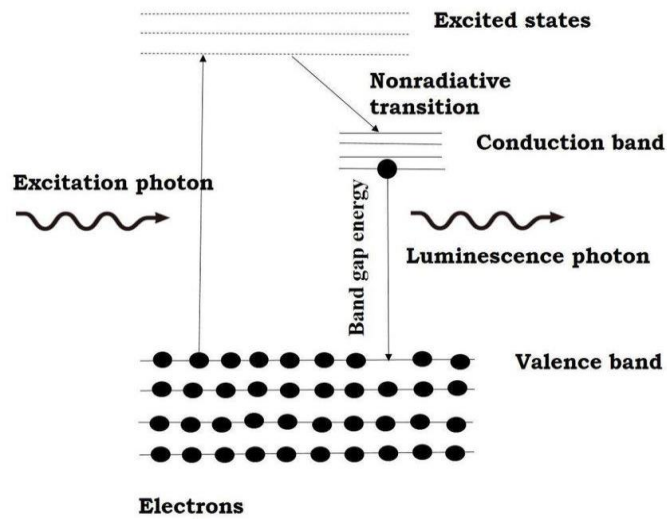
Figure 22: Basic Principle of Photoluminescence Spectroscopy Showing the Excitation of Electrons in Valence Bond to Conduction Band and Recombination.

There are various radiative recombination mechanisms, some of which are depicted in figure 23. Band-to-band recombination involves the transition of a free electron from the conduction band to a free hole in the valence band, occurring at energies equal to or greater than the bandgap. Recombination at energies higher than the bandgap is attributed to "hot carriers" that have not fully relaxed to the bottom (or top) of the conduction (or valence) band prior to recombination. Free electrons and holes can form bound states known as free excitons through Coulomb interaction. Free-to-bound transitions encompass the radiative recombination between a free carrier and an impurity-bound carrier, occurring in two variations: donor-to-valence band and conduction band-to-acceptor. These emissions are predominantly observed at energies below the bandgap. Shockley Read-Hall recombination, characterized by recombination via an intermediary state (e.g., deep level), primarily proceeds non-radiatively. On the other hand, Auger recombination is a three-body process where the recombination energy

is transferred non-radiatively to another particle, such as an electron, in the form of kinetic energy[57].
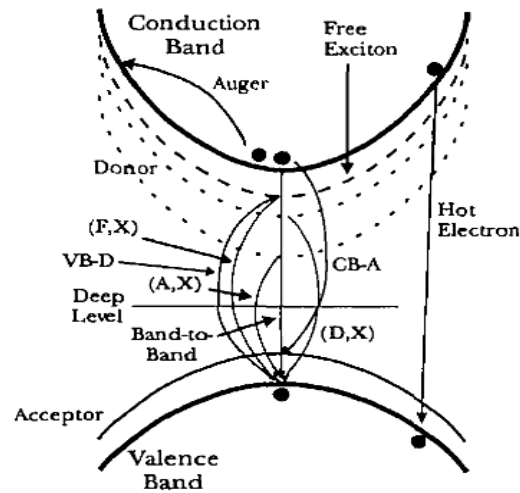
Figure 23: Illustration of Several Possible Radiative Recombination Processes [57].

Furthermore, when performing photoluminescence (PL) measurements at low temperatures, a phenomenon known as the blue shift is observed by Varshini's law (Deutsch, 2012). Varshini's law describes the alteration in the relative positions of the conduction and valence bands resulting from temperature-induced lattice expansion, thereby influencing the interaction between electrons and the lattice. This interaction leads to a reduction in the material's bandgap at lower temperatures. An empirical equation describes the relationship.

$$E_g = E_o - \alpha T^2 \, / \, (T + \beta)$$

Where α and β are material constants, E_o is the band gap at 0 K, and E_g is the band gap at temperature T Kelvin.

The dependence of photoluminescence (PL) intensity on excitation provides valuable insights into the underlying recombination processes [58]. Typically, the PL intensity, denoted as I exhibits a power law relationship with the laser excitation power, P, expressed as $I \propto P\alpha$. The value of α is indicative of the nature of the transition involved. A value of α around 1 suggests an exciton-like transition. At the same time, $\alpha < 1$ indicates recombination pathways involving defects or impurities, such as free-to-bound transitions (recombination between a free hole and a neutral donor or between a free electron and a neutral acceptor) and donor-acceptor pair transitions[59].

PL spectroscopy of neutron-irradiated samples and pristine samples was done using the Renishaw Raman spectrometer using a He-Cd 488 nm blue laser.

2.3.4   Scanning Electron Microscopy (SEM)

A scanning electron microscope uses high-energy electron interactions to create valuable signals on the surface of solid samples. These signals give information about the sample, such as its morphology (texture), chemical composition, crystal structure, and orientation of the crystals in the sample. The electron beam moves in a pattern of lines, and the beam's position and the signal's strength make an image [60]. There are different types of signals, such as secondary electrons (SE), backscattered or reflected electrons, X-rays with specific characteristics and light (CL) from the cathode (cathode luminescence), current that is absorbed, and electrons that go through. All SEMs have detectors for secondary electrons, but not all SEMs have detectors for all the other signals.

In a usual SEM, an electron gun with a cathode made of tungsten filament makes an electron beam [61]. The electron beam has an energy between 0.2 KeV and 40 KeV and is focused on a small spot between 0.4 nm and 5 nm in size using one or two lenses called condenser lenses. The beam goes through pairs of coils that scan or pairs of plates that

deflect in the column of electrons, usually in the last lens, which makes the beam move in the x and y directions so that it covers a rectangular area on the surface of the sample. When the primary electron beam touches the sample, the electrons lose energy by scattering and being absorbed many times in a shape like a drop of water called the interaction volume, which ranges from less than 100 nm to about 5 μm into the surface. The interaction volume depends on how much energy the electrons have when they land, how many protons the atoms in the sample have, and how dense the sample is. The energy exchange between the electron beam and the sample makes some high-energy electrons bounce back by scattering without losing energy, some low-energy electrons come out by scattering and losing energy, and some electromagnetic radiation comes out, each of which can be measured by detectors[61].

The most usual way of making images uses low-energy (<50 eV) secondary electrons that come out from the atoms in the sample by scattering and losing energy with electrons from the beam. These electrons come from a few nanometers below the sample's surface[61]. Backscattered electrons (BSE) are high-energy electrons that come from the electron beam and return from the interaction volume by scattering without losing energy with atoms in the sample. Because atoms with more protons (high atomic number) return more electrons than atoms with fewer protons (low atomic number) and look brighter in the image, BSEs differentiate the contrast between areas with different chemical compositions[61].
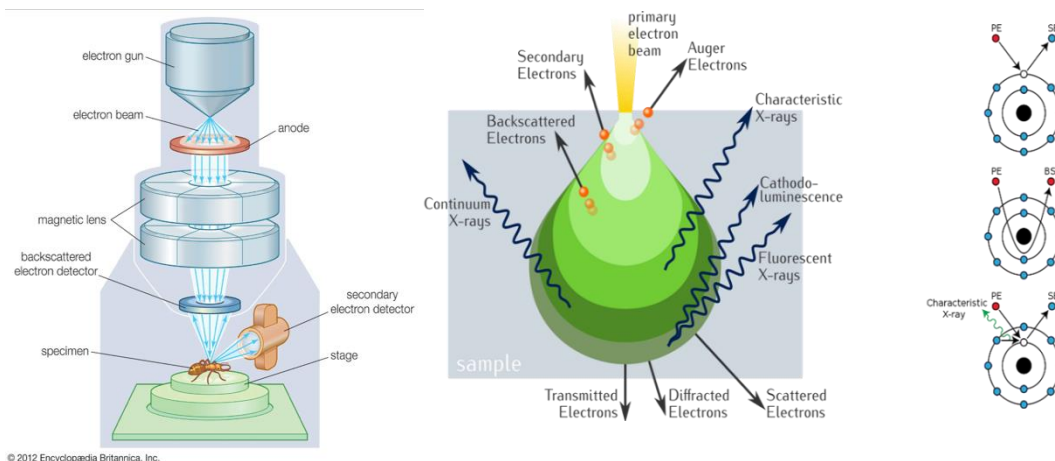
Figure 24: Schematic of SEM [ref: Britannica Inc].

The X-rays emitted from the sample after high-energy electron bombardment are characteristic of the elemental concentrations of the sample. The high-energy electrons may make an electron in a shell close to the nucleus come out from the shell and leave a hole where it was. An electron from a shell farther away from the nucleus then fills the hole, and the difference in energy between the two shells may come out as an X-ray. A detector that filters X-rays based on their energy measures the counts and energy of the X-rays that emit from a sample. Because the energies of the X-rays depend on the difference in energy between two shells and on how many protons are in each element, this device can measure what elements are in the sample[62].

2.3.5 Atomic Force Microscopy (AFM)

Atomic force microscopy (AFM) is widely used in metrology for precise surface roughness and topology measurements. It offers the capability to quantitatively assess surface features in the x, y, and z directions with nanoscale resolution and high precision. In contrast to other high-resolution microscopic techniques like scanning electron

microscopy (SEM) or transmission electron microscopy (TEM), which rely on electron-material interactions and may potentially damage the sample if precautions are not taken, AFM operates by establishing direct mechanical contact between the tip and the sample. This enables accurate characterization of the sample's surface morphology. Various parameters are available to evaluate the surface roughness of the sample qualitatively.
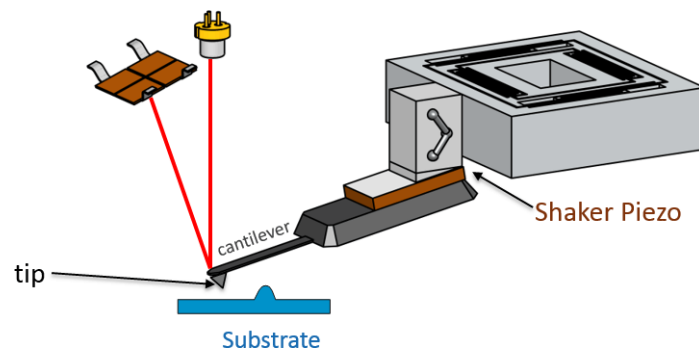
Figure 25: Schematic of AFM [ref: nanosurf].

The working principle of atomic force microscopy (AFM) is centered around the interaction between a cantilever (tip) assembly and the sample's surface. These cantilever tips are typically fabricated from silicon or silicon nitride and possess a conductive or non-conductive coating at the tip region, depending on the specific application. The AFM probe engages with the sample by employing a raster scanning motion across the substrate. A laser beam is directed onto the top of the cantilever, enabling the monitoring of both vertical and lateral movements of the AFM tip as it traverses the surface. This laser beam reflection is captured by a position-sensitive photodetector (PSPD), which detects the sideways and the up-and-down motion of the cantilever. The probe is installed within a holder featuring a shaker piezo to facilitate AFM modes like tapping, as illustrated in figure 25. Tapping mode operations are typically conducted in resonant modes, where the operation is performed at or near the cantilever's resonance frequency.

44

2.3.6   Ultra Violet-Visible (UV-Vis) Spectroscopy

UV-Vis spectroscopy is an analytical technique that measures the absorption or transmission of a sample as compared to a reference or a blank sample. Finding defects at particular wavelengths in a sample is a quick and relatively inexpensive technique. Instruments are equipped with two lamps to measure UV and visible light: a tungsten or halogen lamp for the visible range and a deuterium lamp for the UV range. The instrument switches the light source during measurement to scan different wavelengths. A monochromator selects a narrow band of wavelengths from the light source using a diffraction grating that can be rotated to change the angle of incidence and reflection. The diffraction grating has many grooves per mm, which affect the optical resolution and the wavelength range. For UV-Vis spectroscopy, the groove frequency is usually between 300 and 2000 grooves per millimeter, with at least 1200 grooves per millimeter typical.

2.3.6.1   Sample Analysis

The light from the monochromator passes through a sample, which absorbs some of the light. A reference or "blank sample" is also measured to get accurate absorbance values. The reference sample is similar to the sample but without the substance of interest. The instrument uses the reference sample signal to correct any background absorption.

Some factors, such as the materials and conditions used, can affect the UV-Vis spectroscopy measurements. Plastic cuvettes are unsuitable for UV absorption studies because they absorb UV light. Glass cuvettes can also filter out some UV light, especially UVC and UVB. Quartz cuvettes are preferred for UV measurements because they are transparent to most UV light. Air can also absorb light below 200 nm, so a unique setup with pure argon gas is needed for measurements in this range.[63]

45

2.3.6.2 Detection

After passing through the sample, the light reaches a detector that converts it into an electronic signal that a computer or a screen can read. Different types of detectors are based on photoelectric coatings or semiconductors.

Photoelectric coatings emit electrons when they are exposed to light. The electrons create an electric current that is proportional to the light intensity. A typical detector based on photoelectric coatings is a photomultiplier tube (PMT), which amplifies the electrons to generate a larger current. PMTs help detect deficient levels of light. [63]. Semiconductors allow an electric current to pass through when exposed to light. Two standard detectors based on semiconductors are photodiodes and charge-coupled devices (CCDs). They also produce a current that is proportional to the light intensity. [63]

3. NEUTRON TRANSMUTATION DOPING

When atomic nuclei are bombarded with neutrons, depending on the energy of the neutrons, there is a chance that some of these neutrons are captured. They make nuclei unstable by increasing the mass-energy and neutron-to-proton ratio. The nucleus goes to a higher excited state called resonance state and releases its energy by emitting high-energy photons or Gamma rays, bringing it to an intermediate metastable state ($^{A+1}_{Z}X$ in figure 26).
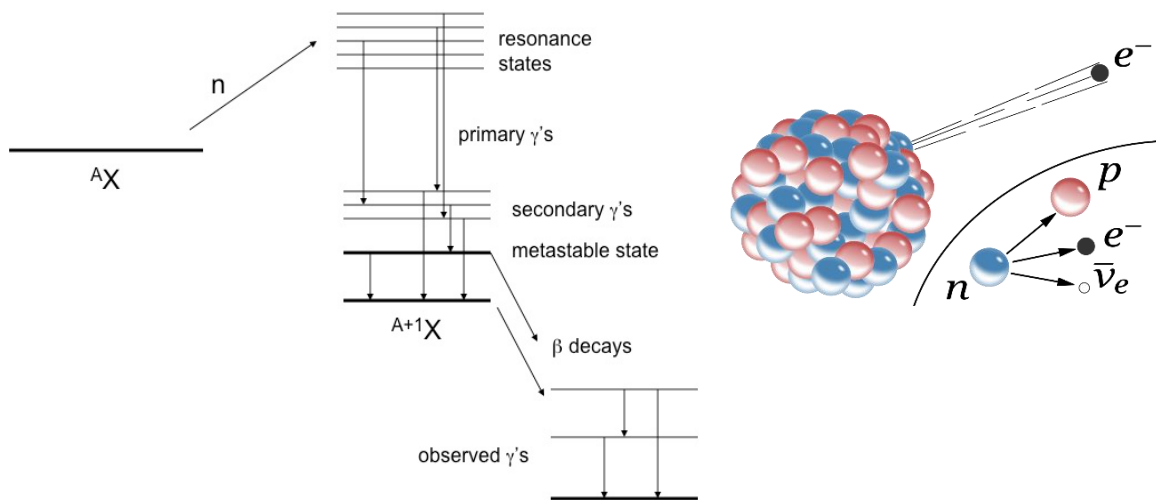
Figure 26: Neutron Capture Process and Beta Decay.

Heavy atoms may undergo additional transitions to reach a metastable state, and in the case of higher isotopes of the same element, beta decay occurs. During beta decay, the nucleus emits a fast-energetic electron or positron, known as a beta particle, transforming into an isobar of the nuclide. When neutron irradiation affects observationally stable isotopes, β- decay is typically observed. This type of beta decay

involves the transformation of a neutron into a proton through the emission of an electron along with an antineutrino ($\bar{\nu}_e$)[64] The parent atom undergoes a transmutation to a different atom with an atomic number increase of 1. E.g., [186]W, one of the stable isotopes of tungsten with a relative abundance of 30.6%, transmutes to Re-187 by neutron capture, emitting gamma (γ) and beta radiation ($e^- + \bar{\nu}_e$) in the process (eq 2)

$$\frac{A}{Z}X + n^0 \rightarrow {}^{A+1}_{Z}X + \gamma \rightarrow {}^{A+1}_{Z+1}Y + e^- + \bar{\nu}_e + \gamma$$

$$\frac{A}{Z}X + n^0 \rightarrow {}^{A+1}_{Z}X + \gamma \rightarrow {}^{A+1}_{Z+1}Y + e^- + \bar{\nu}_e + \gamma$$
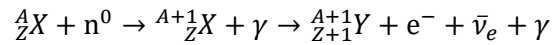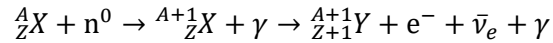
3.1. Selecting Energy of Neutrons

The neutron Transmutation Doping technique is based on the mechanisms of nuclear transmutations mentioned above. Herein we select semiconductors with isotopes that will capture a neutron efficiently. The neutron's energy plays a significant role in determining whether nuclei will capture it. Hence, we have to understand neutron capture to optimize efficient doping. Neutrons have a neutral charge and a mass slightly higher than protons. The same elements which have different neutron numbers are called isotopes. Since they have no charge, they only interact with subatomic particles with weak magnetic movements. Due to the absence of any Coloumbic barrier, neutrons are captured by the nucleus very efficiently.

The neutron capture cross-section (σ_C) is the probability of neutron absorption by atomic nuclei. Essentially, it is the area where the number of neutron-nuclei reactions occurs. The SI unit for measuring the cross section is 'Barns,' which equals 10^{-28} m^2 or 100 fm^2. The larger the neutron cross-section, the more likely a neutron will react with the

nucleus. Let us look at the example of neutron capture cross sections in a Selenium isotope (figure 27).
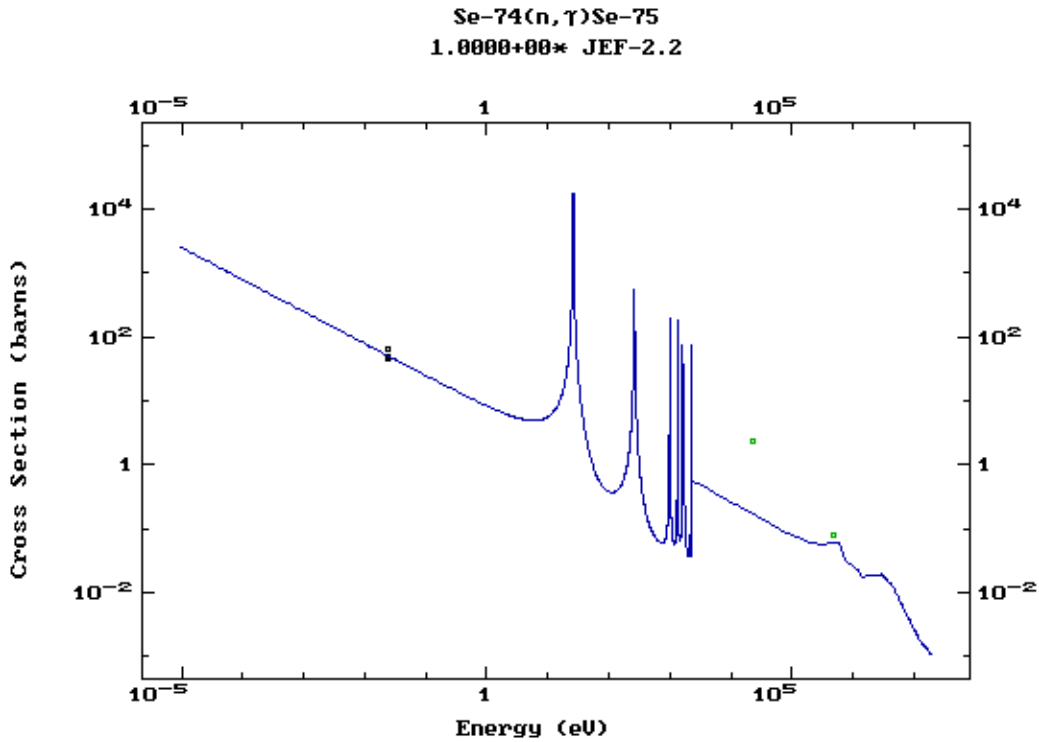
Figure 27: Cross Section of [74] Se vs. Energy[65].

The cross sections at energy levels below 1eV show a linear decrease and are inversely proportional to the energy. Assuming there is no change in the mass of incident neutrons, we can derive that σ_C is linearly proportional to the inverse of velocity as shown in eqn 2

$$\sigma_C \sim \frac{1}{\sqrt{E}} \sim \frac{1}{v}$$

The energy of neutrons corresponding to this transition is also the energy of neutrons at room temperatures, termed thermal neutron energy. The capture sections of

higher energy electrons (non-linear relation to velocity) can be expressed as a function of thermal neutron capture (σ_o), and resonance integral (RI) of higher energy neutrons[65] The RI term considers the sum of all the contributions of higher neutron energies. Resonance integrals are considered mostly in epithermal neutrons as they quickly drop in value for higher energy neutrons, in line with theoretical predictions that highly energetic neutrons will not be captured due to their tendency to collide with incident atoms. The neutron energy and their range are shown in table 1 below:

Table 1: Neutron Energy Ranges [67].

Neutron energy (eV)	Energy Range
0.0 − 0.025	Cold (slow) neutrons
0.025	Thermal neutrons (at 20°C)
0.025−0.4	Epithermal neutrons
~~1–20 MeV~~0.0001-0.0020	Fast neutrons

Efficient neutron doping depends on efficient neutron capture, and ideally, it is expected that most of the neutrons are captured, which gives us very high control over doping levels, with neutron flux as one of the tuning parameters. Hence, it is required that neutron energies are maintained in the thermal range to minimize scattering and defects due to collisions and maximize capture.

3.2. Selecting Candidates for Neutron Doping

The previous section shows neutron transmutation doping depends on the thermal neutron capture cross-section. Hence the number of atoms that capture neutrons and undergo transmutation can be given as follows:

$$N = N_T\, \sigma_0\, \varphi\, t$$

Where N_T is the thermal neutron flux, which is expressed as the number of neutrons/cm^2.s, σ_0 is the thermal neutron capture section (barns), φ is the relative abundance of a particular isotope (unitless), nd ts the time of irradiation (seconds). As per the above equation, the ideal candidates for transmutation doping

3.3. TRIGA Reactor for Sample Irradiation

The average worker in a semiconductor research atmosphere is not trained to handle samples with higher irradiation, especially in a university research setting where only mildly radioactive materials are allowed to handle. Nuclear reactor settings used in this process must be safe and reliable. GA's TRIGA® (Training, Research, Isotopes, General Atomics) reactor is the world's most widely used non-power nuclear reactor. These reactors are operated at thermal power levels from less than 0.1 to 16 megawatts[66]. It was designed by renowned physicists Freeman Dyson and Edward Teller. The TRIGA reactor uses uranium zirconium hydride (UZrH) fuel, which has a high negative fuel coefficient. As the reaction temperature increases, the overall reactivity will go down.
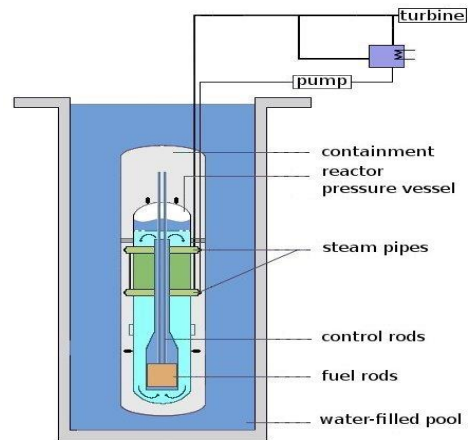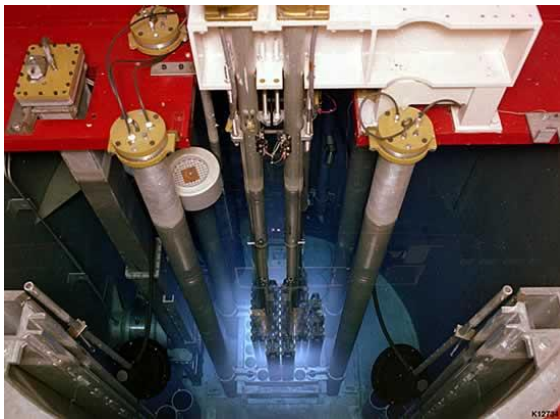
Figure 28: TRIGA Reactor.

The composition of Zirconium Hydride is carefully selected based on desired thermal to fast neutron ratio. ZrH is a rich source of Hydrogen which acts as a neutron moderator.

The most common form of Hydrogen, also known as Protium (H-1), has a neutron capture cross-section enough to moderate the speed of neutrons but not enough to absorb them. This experiment used a 20% Zirconium Hydride + enriched uranium fuel, resulting in a 3×10^{12} cm^{-2}.s^{-1} neutron flux with a very high thermal to fast neutron ratio of 25:1. The vdw crystals used in these experiments are WSe_2, WS_2, InSe, and In_2Se_3, and the time of irradiation is kept as low as 1 hour to avoid very high radioactivities.

3.4. Relative abundances and Neutron Capture Sections of elements

NTD works efficiently if isotopes of higher relative abundance also have significant neutron capture. From a semiconductor defect viewpoint, it is essential to know all the decaying isotopes and their mechanisms to ensure minimal unwanted isotopic defects act as compensators for induced defects. For example, in the NTD process of WSe_2, one of the lower mass isotopes of Selenium Se75 undergoes electron capture (EC) to form As75, a p-

52

type dopant acting as an acceptor. Table 2 represents all the possible decay schemes that will happen during the irradiation of our samples.

Table 2: Isotopes of Elements from The Samples Irradiated with Their Relative Abundance, Half-Life, Type of Decay, and Decay Products[69].

Isotope	Relative Abundance (%)	Neutron Capture section (barns)	Half-life	Mode of decay	Product
Isotopes of Tungsten					
^{180}W	0.12	22.3± 1.7	1.8×10^{18} y	α	^{176}Hf
^{181}W	syn	No data	121.2 days	EC	^{181}Ta
^{182}W	26.5	19.9± 0.3	Observationally Stable		
^{183}W	14.3	10.4± 0.2	Observationally stable		
^{184}W	30.64	1.73± 0.09	Observationally stable		
^{185}W	syn	3.0± 0.3	75.1 days	β−	^{185}Re
^{186}W	28.43	38.1± 0.5	Observationally stable		
^{187}W	syn	64± 10	23.72 h	β−	^{187}Re
Isotopes of Selenium					
^{74}Se	0.86	52.2±0.8	Observationally stable		
^{75}Se	syn		119.78 days	EC	^{75}As
^{76}Se	9.23	84.8± 5.2	Observationally stable		
^{77}Se	7.60	41.5± 4.2	Observationally stable		
^{78}Se	23.7	0.43±0.02	Observationally stable		
^{79}Se	Trace		3.27×10^{5} y	β−	^{79}Br
^{80}Se	49.8	0.593± 0.046	Observationally stable		
^{82}Se	8.82	0.044± 0.003	1.08×10^{20} y	β−β−	^{82}Kr
Isotopes of Indium					
^{113}In	4.28	12.0± 0.6	Observationally stable		
^{114}In	syn	No data	71.9 s	β+ (0.5%)	^{114}Cd
				β− (99.5%)	^{114}Sn
^{114m}In (metastable)	syn	No data	49.5 days	IT (96.75%)	^{114}In
				β+ (3.25%)	^{114}Cd
^{115}In	95.7	202	4.41×10^{14} y	β−	^{115}Sn
^{115m}In (metastable)	syn	No data	4.48 h	IT (95%)	^{115}In
				β− (5%)	^{115}Sn
^{116}In	syn	No data	14.1s	β−	^{116}Sn
Isotopes of Sulfur					
^{32}S	94.8	0.518± 0.014	Observationally stable		
^{33}S	0.76	0.454 ± 0.025	Observationally stable		
^{34}S	4.37	0.25± 0.009	Observationally stable		
^{36}S	0.02	0.23± 0.006	Observationally stable		

Some additional types of decay are mentioned in Table 2:

α: Type of decay in which nuclei emit alpha particles (He nucleus), forming products that have atomic mass reduced by four and atomic number reduced by two

EC: Electron Capture in which the extra proton of a nucleus captures inner shell electrons and transmutes them to neutrons, followed by emission of electron neutrino (ν_e). Atomic mass stays the same, but atomic number increases by one

β⁻β⁻: Double beta decay in which two neutrons are captured simultaneously into two protons and two electrons, increasing the atomic number by two

β⁺: Positron emission, or beta plus decay, a subtype of beta decay in which a proton is converted into a neutron while releasing a positron (e^+) and electron neutrino (ν_e)

IT: Isomeric transition or internal transition is the decay of excited nuclei to low energy state by emission of γ (gamma ray or high energy photon) [67]

3.5. Gamma Ray Spectroscopy Post Irradiation

After irradiation, the target nucleus changes into a new isotope with one more nucleon after capturing a neutron. It reaches an excited state and needs to release energy to become stable. This energy release usually takes the form of high-energy photons called gammas. The time it takes for this energy release can vary. Some gammas are emitted quickly (prompt gammas), while others take longer and have a measurable half-life when the emission rate decreases by half. The gamma emission spectrum shows the nuclear energy levels of the transformed target nuclei. It can be used for a powerful trace substance technique called neutron activation analysis (NAA), which can detect impurity levels as low as 10^9 atoms/cm^3. Each emission line corresponds to a specific nuclear transition of a specific isotope.

The energy and intensity of the gamma rays depend on the neutron-capturing material and the neutron source. Different radioisotopes emit a characteristic gamma while they decay and represent unique gamma-ray spectra after neutron capture. The gamma rays emitted by the neutron-capturing isotopes can be detected by high-resolution germanium or scintillation detectors[68]. The gamma-ray spectra can provide information about the elemental composition and concentration of the sample with great accuracy.
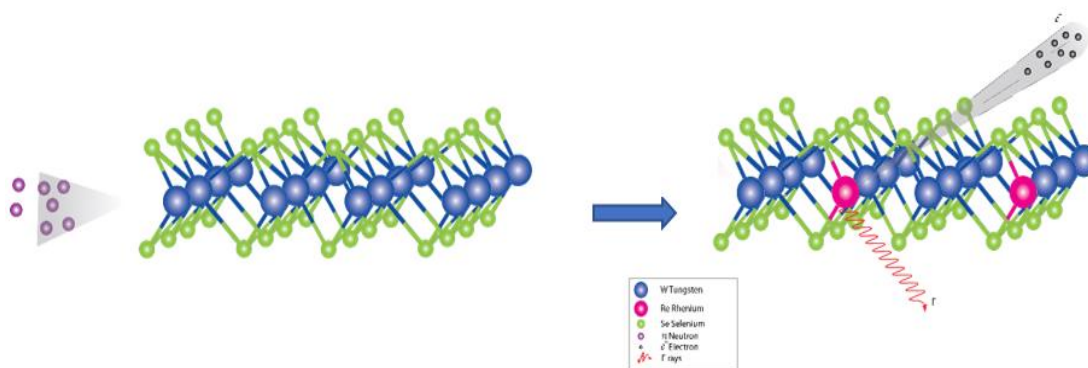
Figure 29: Neutron Transmutation Doping in WSe_2 Crystal.

3.6. High Purity Germanium (HPGe) Detectors in Gamma Measurement

High-purity germanium (HPGe) detectors are optimal for accurate gamma and x-ray spectroscopy. Germanium outperforms silicon in detecting high-energy radiation due to its higher atomic number and lower energy requirement for creating an electron-hole pair. Silicon has 3.6 eV, whereas germanium only needs 2.9 eV[69]. The higher atomic number of germanium also results in more significant gammas absorption, leading to a shorter mean free path. In contrast, silicon detectors are limited to a thickness of a few millimeters, while germanium detectors can reach a centimeter scale. This allows them to detect higher volumes of samples and increases accuracy. To achieve maximum efficiency, HPGe detectors must operate at extremely low temperatures of liquid nitrogen (-196 °C).

Cooling the detectors minimizes the noise caused by thermal effects, enabling optimal performance.
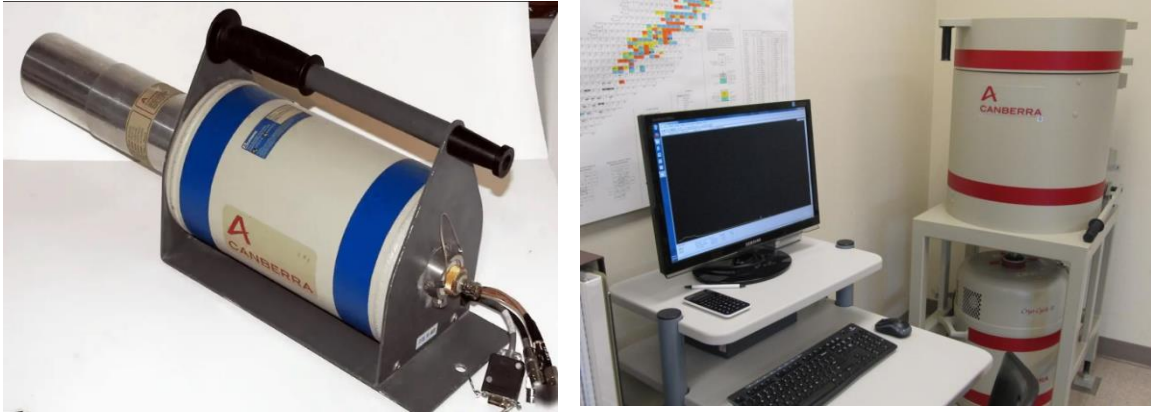
Figure 30: a HPGe Detector Probe. **b** HPGe Setup with Liquid Nitrogen Dewar and Computer-Based Analysis System[73].

An electric field within the detector causes the electrons and holes to move toward the respective electrodes. This movement results in the generation of a pulse, which can be measured using an external circuit. The pulse carries valuable information about the energy of the incident radiation. Additionally, the number of pulses per unit of time provides insights into the intensity of the radiation.

In all scenarios, a photon transfers a portion of its energy along its path and can be completely absorbed. For instance, the absorption of a 1 MeV photon generates approximately 3×10^5 electron-hole pairs[69]. However, this value is relatively small compared to the total number of free carriers per unit cubic centimeter.
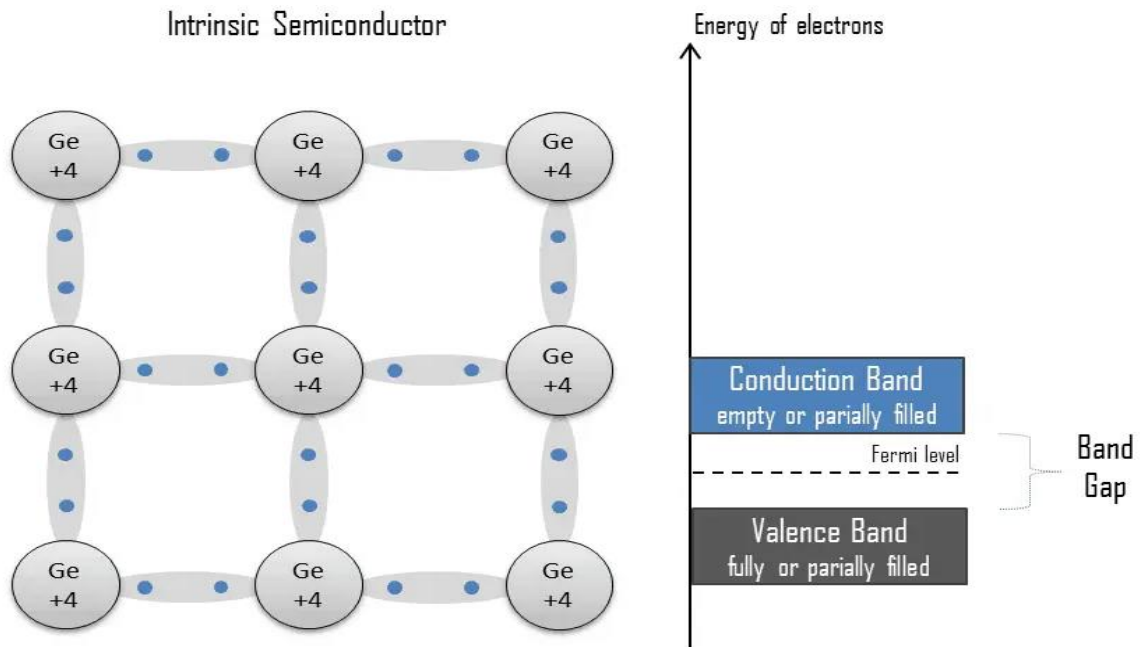
Figure 31: Electronic Structure of Intrinsic Ge Semiconductor.

3.7. Detector Efficiency Curve

A traceable source that emits gamma rays at various energies is placed in a fixed position relative to the detector to calibrate a gamma-ray spectrometer. A spectrum is then recorded from this arrangement. The measured spectrum and the source calibration certificate (figure 32), which specify the source activity (a) and calibration date, compute the efficiency (μ) of the detector at each energy level emitted by the source in that specific position. This efficiency is derived from a polynomial curve fit that relates the detector's efficiency and the energy of the gamma rays.

Figure 32: Detector Efficiency Curve and Certification of Calibration Sources.
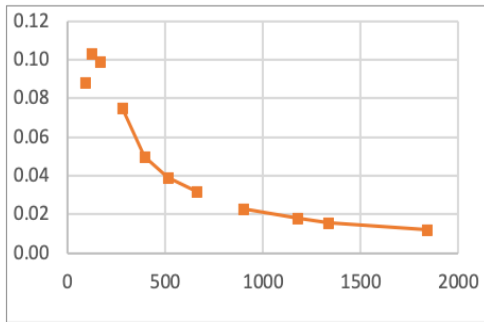
Gamma-Ray Energy (keV)	Nuclide	Half-life	Branching Ratio (%)	Activity (µCi)	Gammas per second	Total Uncert.
88	Cd-109	462.6 ± 0.7 days	3.63	2.142	2877	3.0 %
122	Co-57	271.79 ± 0.09 days	85.6	0.08517	2698	3.0 %
166	Ce-139	137.640 ± 0.023 days	79.9	0.1103	3261	3.0 %
279	Hg-203	46.595 ± 0.013 days	81.5	0.2983	8995	3.0 %
392	Sn-113	115.09 ± 0.04 days	64.9	0.4114	9879	3.0 %
514	Sr-85	64.849 ± 0.004 days	98.4	0.5187	18880	3.0 %
662	Cs-137	30.17 ± 0.16 years	85.1	0.3711	11680	3.0 %
898	Y-88	106.630 ± 0.025 days	94.0	0.8339	29000	3.0 %
1173	Co-60	5.272 ± 0.001 years	99.86	0.4381	16190	3.0 %
1333	Co-60	5.272 ± 0.001 years	99.98	0.4381	16210	3.0 %
1836	Y-88	106.630 ± 0.025 days	99.4	0.8339	30670	3.0 %

The stated 3-sigma uncertainty (at 99% confidence) for each peak in the source's emission rate is 3%.

$$N = a\,b\,\mu\,t$$

Here, N is the number of counts at a particular energy; a is the test sample's activity (number of disintegrations per second); b is the branching ratio of the isotope; t is the counting time interval. This calculation also compensates for the effects of the dead time of an isotope and the uncertainties caused by it. The next step involves determining the activity of the calibration sources using exponential decay.

$$a = a_0 e^{-\lambda \cdot t}$$

Here, a_0 represents the initial activity, λ the decay constant, and t is the elapsed time since the source's initial calibration. The initial activity is known, while the half-lives and branching ratios are obtained from reliable isotope data sheets compiled by vendors. Once the detector efficiency was calculated for the three detectors and their corresponding test isotopes, an Excel data plot was generated to visualize the efficiencies at different energy levels. Notably, it was found that utilizing a logarithmic scale allowed for a reasonably linear fit in the high-energy gamma-ray range.

$$\mu = c.E_n^d$$

$$\ln \mu = \ln c + d.\ln E_n$$

Here, c represents a coefficient required for the fit, n is the subscript denoting the isotope being used, and d is a power term necessary for the fit.[70]

Pristine samples were placed in a nuclear reactor just below the core centerline and were irradiated for one hour. The neutron flux where the samples were located was determined to be 2.8×10^{12} neutrons per centimeter squared per second. Bulk crystals were placed in the reactor so that the neutrons would arrive, traveling parallel to the layers of each crystal. This was done to lessen the possibility that different layers in the same crystal would have different dopant concentrations. Samples were allowed to decay for 15 days after being irradiated, as they were too radioactive to be safely handled until this point.

The two major naturally-occurring isotopes of tungsten are W_{184} (30.7 at.%) and W_{186} (28.6 at.%). W_{184} transmutes to W_{185} upon neutron capture, which decays to Re_{185} via β-decay ($T_{1/2}$ = 75.1 days). W_{186} transmutes via neutron capture to W_{187}, which decays to Re_{187} via β- decay ($T_{1/2}$ = 23.72 hours). The production rate of W_{185} and W_{187} from neutron irradiation depends primarily on the energy spectrum of the incoming neutrons. Neutron absorption cross sections for tungsten isotopes vary significantly, by eight orders of magnitude (up to 10 kbarns), for varying neutron energy in the 1 eV to 14 MeV range.

Meanwhile, the neutron absorption cross-section for a given energy can differ by up to five orders of magnitude due to the presence of resonances. Irradiation of tungsten

at different neutron energies and flux is expected to produce different amounts of rhenium. The transmutation reaction of tungsten by thermal neutrons can be described as:

$$^{184}_{74}W(n, \Gamma) \rightarrow {}^{185}_{74}W(n, \Gamma) \rightarrow {}^{185}_{75}Re \text{ (β decay)}$$

$$^{186}_{74}W\ (n, \Gamma) \rightarrow {}^{187}_{74}W(n, \Gamma) \rightarrow {}^{187}_{75}Re \text{ (β decay)}$$
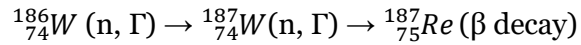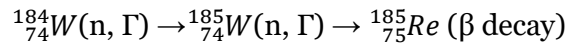
Previous studies indicate that the primary reaction when In$_2$Se$_3$ is irradiated with neutrons is the transmutation of In$_{115}$ (natural abundance of 95.7%) to In$_{116}$, followed by β-decay to Sn$_{116}$. The transmutation of In$_{115}$ by thermal neutrons can be described as:

$$^{115}_{49}In(n, \Gamma) \rightarrow {}^{116}_{49}In(n, \Gamma) \rightarrow {}^{116}_{50}Sn \text{ (β decay)}$$
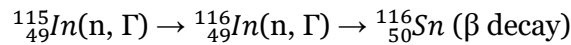
The tungsten and indium decay mechanisms described above are illustrated in figure 33.
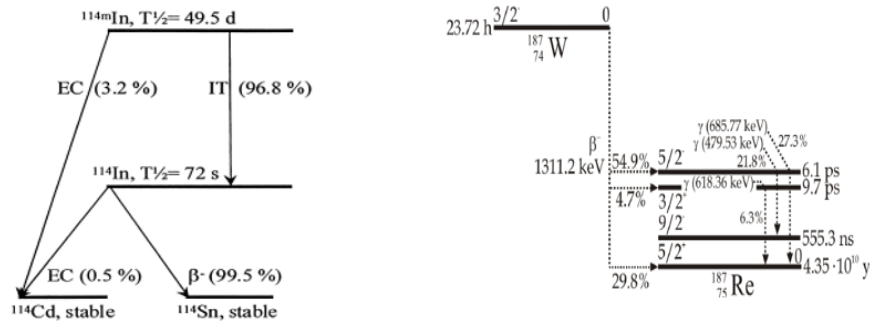
Figure 33: Nuclear Decay Mechanisms for Indium (left) and Tungsten (right) Isotopes Produced When Their Respective Samples are Irradiated with Thermal Neutrons.

3.8. Determining Dopant Concentration after NTD

After samples were removed from the nuclear reactor, neutron activation analysis using gamma-ray spectroscopy was used to determine the level of doping achieved. This method detects dopants indirectly; the signal comes from the decay of radioactive isotopes ($^{185}_{74}W$, $^{187}_{74}W$, and $^{114}_{49}In$) which produce the dopants, so additional calculations are required to determine the exact concentration of dopants. Acquired gamma spectra are shown in figures 34-35. The activities (in Becquerel) of the prominent isotopes were calculated by carefully analyzing the peak positions, deconvolution of minor peaks, and fitting the peaks using Visual RobFit (VRF) formalism.

3.9. Activity Corrected for Decay During Acquisition

The value of the activity of a decaying radionuclide at the beginning of spectral acquisition is desired. If the decay constant of the radionuclide is λ, the real-time spectral acquisition is T_A, and the uncorrected activity averaged over time as determined from the spectral data is A_U.

$$A_A = A_U \frac{\lambda T_A}{1 - e^{-\lambda T_A}}$$

The uncertainty of the measured activity is given by:

$$\sigma_{A_A} = \sigma_{A_U} \frac{\lambda T_A}{1 - e^{-\lambda T_A}}$$

Activities were then used, along with the time since irradiation and the half-lives of the radioactive isotopes, to determine the concentrations of rhenium and tin in WSe_2 and In_2Se_3, respectively. These calculations showed 0.004 at. % rhenium doping in WSe_2 and 0.01 at.% tin doping in In_2Se_3
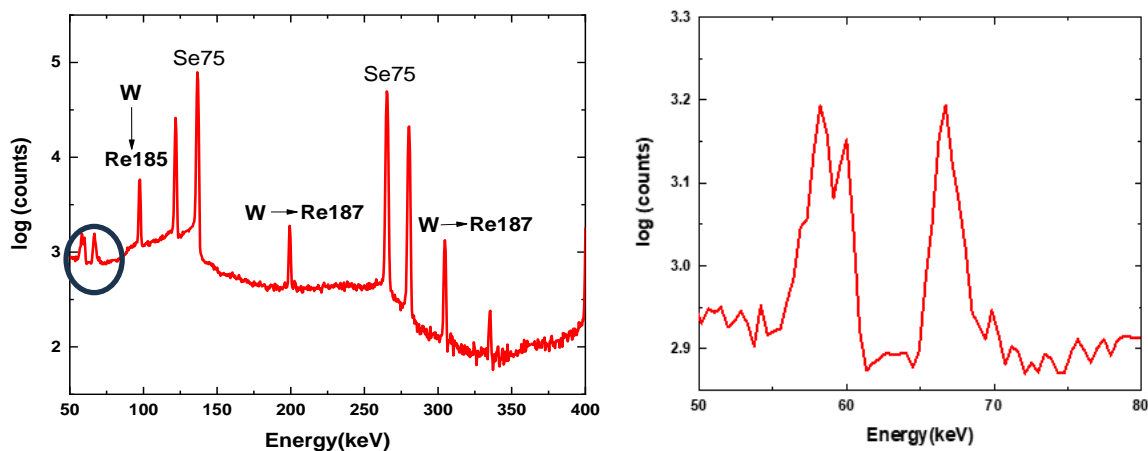
Figure 34: a Gamma Spectrum of WSe_2 Acquired After Thermal Neutron Irradiation. **b** Magnified View of X-Ray Region of the Gamma Spectra Corresponding to Rhenium X-Rays.

The strong presence and activity from W-185 and W-187 is an indication of the transmutation of Tungsten (figure 34 a), and the presence of Rhenium Characteristic X-rays peaks (figure 34 b) corresponding to Kα and Kβ shows us the confirmation of Rhenium in our sample. Since the probability of beta decay of W185 and W187 to Re185 and Re187, respectively, is 1. A comprehensive quantitative analysis of W185 and W187 gamma spectra with individual peak deconvolution and accurate fitting was done using Visual Robfit formalism.

The activity of each isotope from the gamma spectra is reverse decayed to the exact time to irradiation to calculate an accurate number of atoms that undergo transmutation. The number of dopant atoms/cm³ is given by:

$$\text{Atoms/cm}^3 = \frac{\text{Bq} \times t_{1/2}}{\ln{(2)}/V}$$

Where Bq (Becquerel) is the counts or disintegrations per second, $t_{1/2}$ is in seconds, and V is in units of cm³.

In this case, the half-life of W187 is 23.72 hours, which beta decays to Re187 with probability 1. We calculate the hours since sample collection, which is 20.99. Hence, the number of half-lives since sample collection is given by (20.99/23.72) = 0.875. This means the spectrum analysis result for W187 was reverse-decayed by multiplying by 2^0.875 = 1.834.

A summary of the isotopes of interest is given in tables 3 and 4 below where:

1. Columns labeled "Apparent" are activities derived from the spectrum without regard to decay

2. "Uncertainty" is the standard deviation of "Apparent" activity that would result if many spectra of the same source were acquired under the same conditions and analyzed in the same way.

3. "Relative Error" is the ratio of "Uncertainty" activity to "Apparent."

4. Columns labeled "Acquisition" are activities under "Apparent" that have been corrected for decay during the spectrum acquisition.

5. Columns labeled "Collection" are "Acquisition" activities that have been reverse-decayed from the time of sample collection to the start of spectrum acquisition

Table 3: Summary of WSe$_2$ Spectra in Number of Atoms/cm^3 Radionuclides of Interest.

Emitter	Apparent	Uncertainty/Error	Rel. Error	Acquisition	Collection
Re(x-rays)	78248.8	859.74	0.0109	No half life	No half life
W-185	1.17442E16	1.13724E15	0.0968	1.17444E16	1.27804E16
W-187	8.7948E12	2.3298E10	0.00026	8.8074E12	5.4288E15
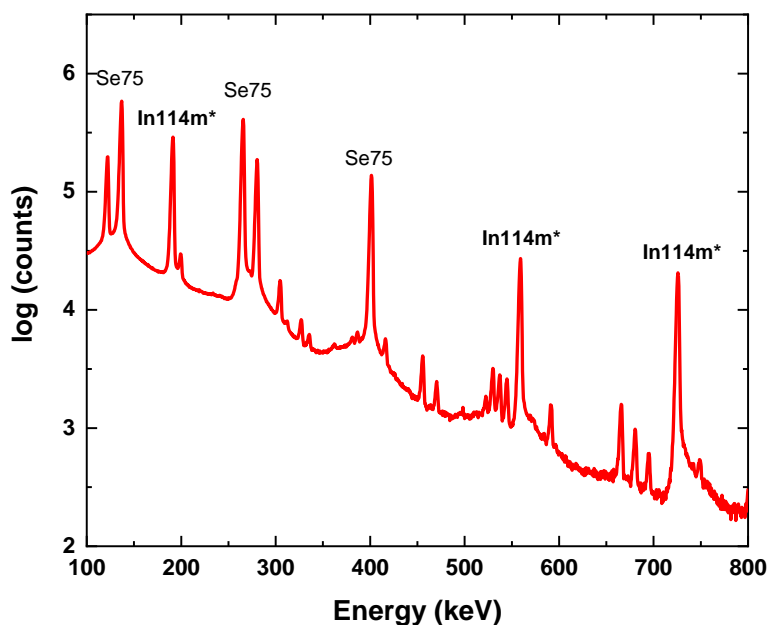
Figure 35: Gamma Spectrum of In$_2$Se$_3$ Acquired After Thermal Neutron Irradiation.

Table 4: Summary of In$_2$Se$_3$ Spectra in Number of Atoms/cm^3 Radionuclides of Interest.

Emitter	Apparent	Uncertainty/Error	Rel. Error	Acquisition	Collection
In-114m	7.466E14	5.863E11	0.0057	7.466E14	7.572E14
In-115m	3.640E12	1.783E9	0.0035	3.662E12	2.193E14

The gamma spectra of Indium Selenide can only detect longer-lived In114m and In115m as the half-life of In116, which decays to Sn116, is 57minutes, and it is not possible to measure spectra before a sufficient cooling time. The In116 isotopes decays to Sn116 as follows:

$^{115}_{49}In(n,\Gamma)$ $^{116}_{49}In(n,\Gamma) \rightarrow$ $^{116}_{50}Sn(\beta$ decay)
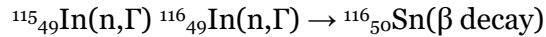
Whereas In114m also decays to stable Sn114 eventually by isomeric transition to In114 followed by a beta decay to Sn114 as shown in figure 33 (right)

3.10. SIMS Analysis of WSe_2

Gamma spectroscopy, a non-destructive technique based on the theory of transmutation, holds the potential for accurately estimating the quantities of dopant atoms and their isotopic concentrations with high precision and minimal relative error. Nevertheless, it poses challenges when measuring isotopes with relatively short half-lives, as their precise quantities can only be determined until the sample reaches a sufficiently radioactive state.

To overcome these limitations, a more direct and reliable approach was employed to measure the concentration of Rhenium dopants using Secondary Ion Mass Spectrometry (SIMS). Figure 36 showcases the SIMS data obtained from pristine and neutron-irradiated WSe_2 samples. A pristine WSe_2 sample (prior to irradiation) was utilized to establish a calibration point for the SIMS analysis. It is crucial to note that conventional methods relying on relative isotopic abundances cannot be deemed entirely dependable when dealing with heavy metals such as Tungsten and Rhenium. This is since

heavier isotopes possess lower velocities, making them more susceptible to collisions during transmission.

In order to ensure accurate and comparable measurements, both the pristine and irradiated samples were subjected to identical vacuum conditions, accelerating voltages, and beam currents, resulting in similar intensity positive ion spectra. The peak area of W-180 in the pristine and irradiated sample was measured to be 0.00156, demonstrating an impressive level of agreement.

Moreover, the absolute intensities (area) at 185 and 187 in the irradiated sample exhibited a noteworthy 45% increase, surpassing the 2σ error margin of 8%. Consequently, this excess intensity is attributed to the presence of Rhenium, as the probability of tungsten ions (H+) forming such a dramatic increase is highly unlikely.
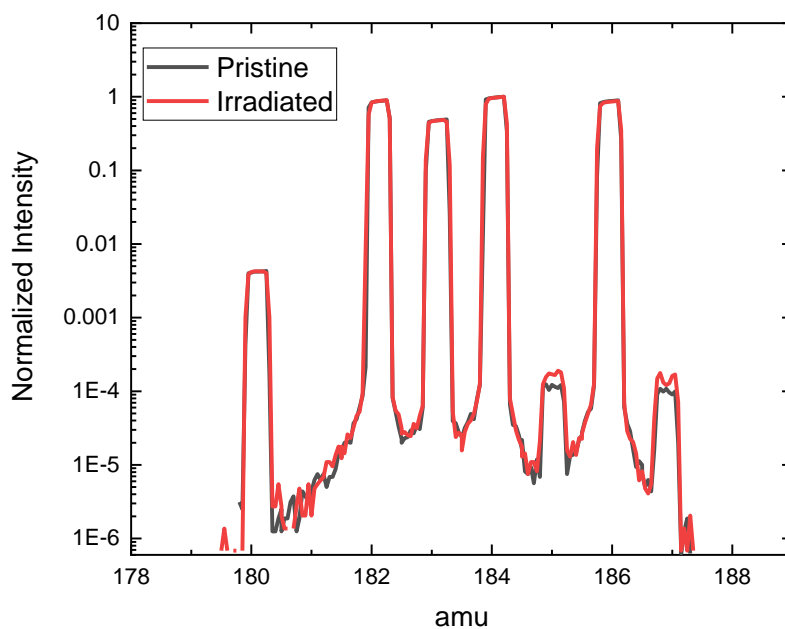
Figure 36: SIMS Spectrum from Pristine (Black line) and Neutron-Irradiated (Red Line) WSe_2.

The following procedure was carried out to obtain the concentration of rhenium dopants in WSe_2 after NTD:

1. Expected peak intensity areas for $W_{184}/(WH_{184}^+)$ is calculated from pristine sample (determined to be 8512).

2. Same ratio is calculated from Irradiated sample (determined to be 5381, which is lower than in the pristine sample, indicating the presence of $^{185}_{74}W$ and $^{185}_{75}Re$.

3. Hence, $\frac{W_{184}}{W_{184}H^+} = 8512 \; and \; \frac{W_{184}}{W_{184}H^+ + Re_{185}} = 5381$

4. Solving for $\frac{Re}{W}$ gives us **6.83E-5 or 0.0068% Re**

While the SIMS analysis strongly indicates the presence of Rhenium in the sample, it is essential to conduct further measurements to obtain an accurate and precise concentration of Rhenium. To ensure a comprehensive analysis, the same measurement will be replicated in WS_2. By expanding the investigation to include WS_2, a deeper understanding of the sample's composition and a more comprehensive analysis of the Rhenium dopants can be achieved.

These results suggest that NTD has introduced dopants into WSe_2 and In_2Se_3 on the order of 10^{16}-10^{17} dopants per cm^3.

4. OPTICAL CHARACTERIZATION

Overall, eight different types of samples were irradiated with thermal neutrons and analyzed as mentioned in chapter 3. These included:

1. Exfoliated WSe_2, WS_2 monolayers on SiO_2,

2. WS_2 and WSe_2 monolayers grown using CVD on Sapphire substrate

3. InSe and In_2Se_3 few layers exfoliated on SiO_2 substrate

4. WSe_2 monolayer FET device

5. Bulk crystals of WSe_2, WS_2, InSe, and In_2Se_3

These crystals and monolayers were synthesized as mentioned in Chapter 2 using CVT and CVD techniques respectively. Due to contamination in shipping, nuclear reactor surroundings and operational handling, monolayers exfoliated on SiO_2 substrate were contaminated and caused low quality datasets. CVD grown samples were also contaminated, but monolayers were intact but did not yield good quality datasets.

Lorentzian function for peak fitting:

$$f(x) = \frac{A}{\pi} \frac{\Gamma/2}{(x-)^2 + (\Gamma/2)^2}$$

where A is the area under the curve, x_0 is the peak position, and Γ is the full width at half maximum (FWHM).

A Lorentzian function fits monolayer Raman and PL data efficiently as it can capture the effects of homogeneous broadening caused by the finite lifetime of the excited states involved in the transitions. Homogeneous broadening is independent of the

frequency and proportional to the inverse of the lifetime. The Lorentzian function can account for the strong exciton-phonon coupling in monolayer TMDCs, which leads to phonon replicas in the spectra. Phonon replicas have similar shapes and widths as the main exciton peak but shifted by multiples of the phonon energy[71].

Gamma spectroscopy measurements showed that Si, Al, Au used in electrodes and substrates also undergo beta decays and get affected by neutron induced defects. Doping in substrates also cause some unwanted changes preventing one to one characterization of neutron irradiation on monolayers as compared to pristine monolayers. For instance, WSe_2/SiO_2 has a type-I band alignment with a valence band offset (VBO) of 1.85 eV and a conduction band offset (CBO) of 0.55 eV, while $WSe_2/n-SiO_2$ has a type-II band alignment with a VBO of 1.85 eV and a CBO of -0.45 eV. This means that $WSe_2/n-SiO_2$ has a larger built-in electric field than WSe_2/SiO_2, which can enhance the separation of electron-hole pairs or A exciton energy[72]. Hence, we will focus on top-down approach to understand effects of irradiation on monolayers exfoliated from bulk crystals

4.1. Raman Spectroscopy

The Raman spectra of monolayer WSe_2 are dominated by E' and A'$_1$ modes which are degenerate at 250 cm^{-1} whereas WS_2 is dominated by two first-order peaks assigned as E' (357.7 cm^{-1}) and A' 1 (419 cm^{-1})[73]. The E' and E" modes are in-plane vibrations of W and Se atoms, meaning they vibrate along the monolayer plane. The E' mode is a combination of two degenerate modes that vibrate along x and y directions. In comparison, the E" mode is a combination of two degenerate modes that vibrate along x+y and x-y directions. These modes have higher frequencies than the out-of-plane modes because the in-plane vibrations are stiffer than the out-of-plane vibrations[74].

The A'1 and A1g modes are out-of-plane vibrations of W and Se atoms, projecting a perpendicular vibration to the monolayer plane. The A'1 mode is a symmetric out-of-plane vibration of W and Se atoms, which vibrate in phase. The A1g mode is an antisymmetric out-of-plane vibration of W and Se atoms, which are out of phase. These modes have lower frequencies than the in-plane modes because the out-of-plane modes vibrate more rigorously than the in-plane modes[74].

The Raman spectra of monolayer WSe_2 are dominated by E' and A'$_1$ modes which are degenerate at 250 cm^{-1} [75]. For both 1L WS$_2$ and 1L WSe$_2$, the intrinsic E' mode is usually overlapped by the 2LA(M) mode in the Raman spectra under resonant condition. To get the intrinsic E' and A' 1 modes, the 488 nm excitation is used to obtain the non-resonant Raman signal of these pristine and irradiated.
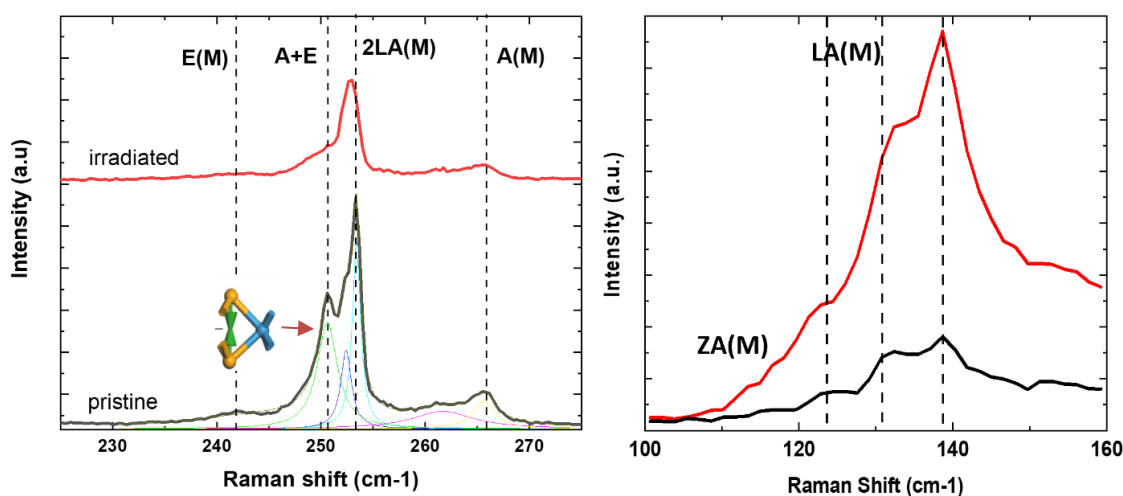
Figure 37: a Raman Spectra of Pristine and Irradiated WSe$_2$ Monolayers (Blue Atoms Shown by Tungsten and Yellow by Selenium in the Ball Stick Model). **b** Low Frequency Raman Spectra to Observe LA Modes of WSe$_2$ Monolayer.

Table 5: Lorentzian Function Based Peak Positions and FWHM of Prominent Peaks.

Pristine		Irradiated	
Xc (cm^{-1})	FWHM	Xc (cm^{-1})	FWHM
130.03 ± 0.38	5.95 ± 1.16	132.03 ± 0.31	4.94 ± 1.16
136.11 ± 0.37	16.42 ± 2.81	138.64± 0.25	7.75 ± 0.88
250.59 ± 0.03	2.34 ± 0.11	249.98 ± 0.12	3.28 ± 0.32
252.39 ± 0.03	1.25 ± 0.14	252.43 ± 0.04	1.31 ± 0.12
253.38 ± 0.01	0.95 ± 0.03	253.16 ± 0.02	0.91 ± 0.08
265.61 ± 0.07	2.55 ± 0.35	265.33 ± 0.10	2.56 ± 0.33

For the irradiated sample the A+E degenerate mode red shifts by ~ 0.5 cm^{-1} and broadens by ~ 1cm^{-1}. The Raman signal of irradiated monolayer is also slightly lower than pristine. This indicates that Neutron irradiation degrades the crystallinity of WSe$_2$ monolayer. Rhenium dopants with their increased atomic mass will break translational symmetry and directly affect the E' mode which is in-plane vibration of W-Se resulting in a redshift and broadening due to increased phonon scattering. However, it is unlikely that such low doping concentrations of Re will cause such changes. At low frequencies some peaks related to LA(M) modes at 130 cm^{-1} and 136 cm^{-1} are more pronounced in the irradiated sample corresponding to the defect activated modes of WSe$_2$[76,77] as shown in figure 37 b.
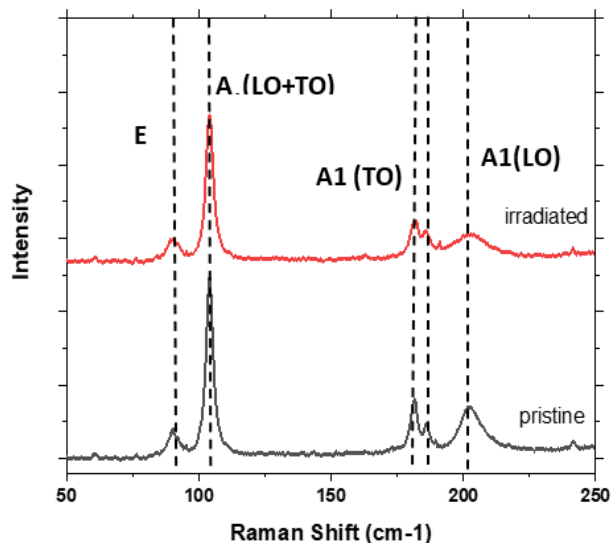
Figure 38: Raman Spectra of In_2Se_3 (Few-Layered) Before and After Irradiation.

Table 6: Lorentzian Function Based Peak Positions and FWHM of Prominent Peaks of In_2Se_3 Raman Spectra.

Pristine		Irradiated		
Xc (cm-1)	FWHM	Xc (cm-1)	FWHM	Mode (Ref [78])
27.54	1.27	27.44	1.39	E
90.03	2.57	89.95	3.06	E
103.95	2.91	103.94	3.00	A1(LO+TO)
181.35	2.95	181.52	3.17	A1(LO)
186.06	2.04	185.93	3.23	A1(TO)
202.95	10.65	202.74	16.3	A1(LO)

The observed Raman modes confirm an α-In_2Se_3 phase of the crystal [79]. Broadening of prominent Raman modes is observed in In_2Se_3 along with slight redshift indicating increased density of defects. Further studies are required to understand the broadening mechanisms in the irradiated crystals.

4.2. PL Spectroscopy

The Room temperature PL spectra shows a 10 meV red shift and 7 meV broadening due to increased phonon-exciton interaction at the defect sites and quenching by 70%. The reduced PL intensity and redshift of irradiated WSe_2 are likely due to an increased density of trions induced by electron doping[30,34,80,81] . For a 532 nm laser, PL spectra taken at 77 K, shows 7 meV neutral exciton red shift and a 5 meV reduction in trion binding energy. No significant defect related photoluminescence was observed. However, the intrinsic defect peaks in the pristine monolayer disappear for the irradiated monolayer, suggesting that irradiation induces defects compensated the intrinsic defects. Since these changes are minimal, several monolayer pristine and irradiated samples (15 each) were prepared to study the neutral exciton peak shift and full width half maximum FWHM.
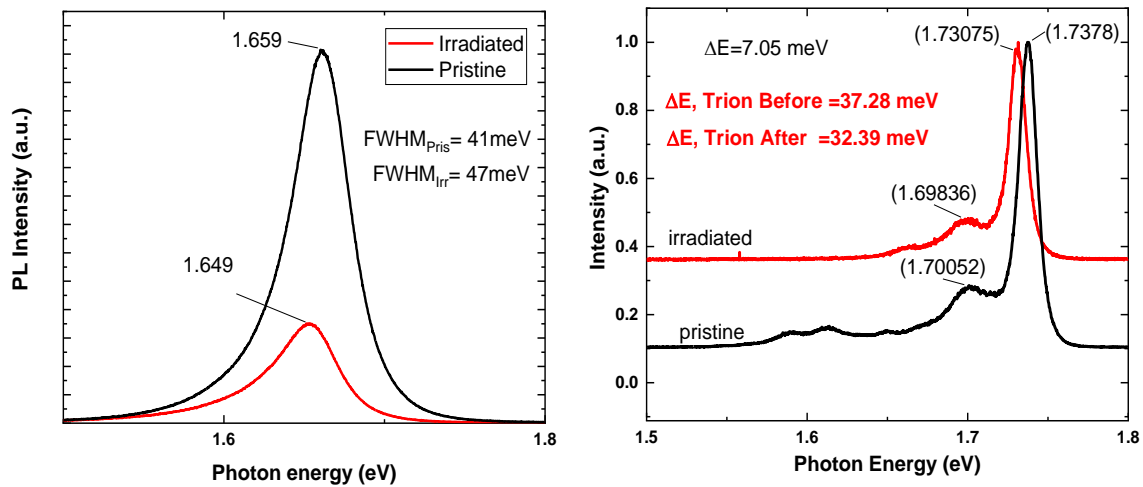
Figure 39: PL Spectra of WSe_2 Monolayer: **a** at Room Temperature and **b** 77 K.
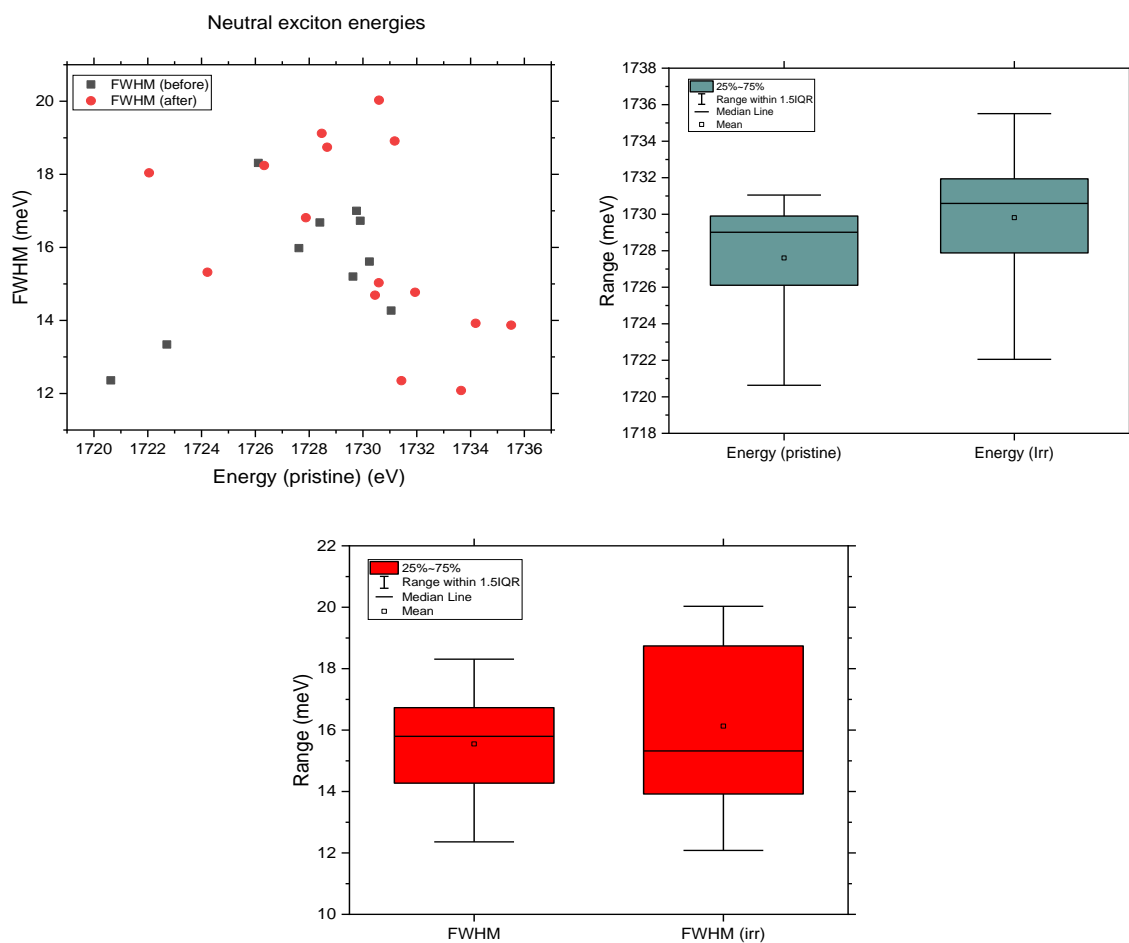
Figure 40: a Scatter Plot of Neutral Exciton Energies for 15 Pristine and Irradiated WSe$_2$ Monolayers **b** Box Plot Showing Neutral Exciton Energies **c** Box Plot of FWHM of Neutral Exciton Peaks.

While Trion energies do not change significantly, neutral exciton energies show slight variation at different spots and monolayers. Statistically, it is seen that the neutral exciton energies show an overall trend of blue shift in mean energies (figure 40 b) and higher broadening range indicating localized variations in defect density (figure 40 c).

4.2.1. Low Temperature PL with 488 nm Laser.

The features seen with low temperature PL were reported previously for ion implantation[74] and alpha particle irradiation [29].

ab
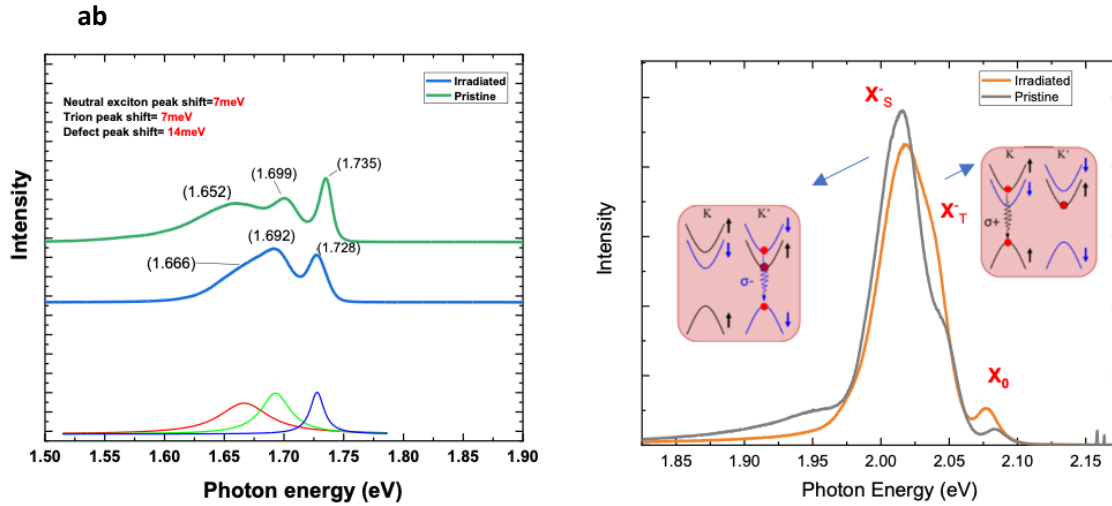
Figure 41: PL Spectra Taken at 77 K for **a** WSe$_2$ Monolayer **b** WS$_2$ Monolayer.

However, no Rhenium related defect peak or feature was observed. Low temperature PL measurements were repeated with a 488 nm laser for both WSe$_2$ and WS$_2$ monolayer.

Table 7: PL Spectra of WSe$_2$ Monolayer at 77 K (488 nm).

Pristine		Irradiated	
Xc (eV)	FWHM (meV)	Xc (eV)	FWHM (meV)
1.652(D)	52.4	1.666(D)	43.7
1.699(X_T^-)	20.4	1.692(X_T^-)	29.1
1.735 (X_0)	11	1.728(X_0)	14.3

In 1L-WSe$_2$, one prominent change was the decrease in binding energy of bound exciton by 21 meV and the decrease in its FWHM by 10 meV. This could be due to the neutron irradiation creating defects in the WSe$_2$ monolayer, such as selenium

75

vacancies. These defects can act as localized states that trap excitons and reduce their binding energy. The defects can also reduce the exciton-phonon coupling and the homogeneous broadening of the bound exciton peak[82]. The bound exciton (D) peak was only seen with 488 nm laser, not 532 nm, implying that the bound exciton requires higher excitation energies.

Table 8: PL Spectra of WS_2 Monolayer at 77 K (488 nm).

Pristine		Irradiated	
Xc (eV)	FWHM (meV)	Xc (eV)	FWHM (meV)
$2.010(X_s^-)$	35.9	$2.019(X_s^-)$	33.1
$2.045(X_T^-)$	10.1	$2.040(X_T^-)$	18.1
$2.081 (X_o)$	25.9	$2.080(X_o)$	3.98

The low temperature PL spectra of WS_2 monolayer (figure 41 b) is a characteristic of interplay between negative trions such as intervalley triplet trion X^{T-} and the intravalley singlet trion X^{S-} which consist in the binding of a photo-generated electron-hole pair with a resident electron from the opposite (same) valley. [83] Post irradiation 9meV blue shift in singlet trion with no change in FWHM, red shift in triplet trion by 5 meV with 8 meV increase in FWHM. Significant decrease in FWHM of X_o observed from 25 meV to 4 meV. The blue shift in singlet trion could also be due to increased electron concentrations[84]. The fact that its FWHM does not change means that its lifetime and quality factor remain constant.

Resistivity measured using four probe measurements in WSe_2 bulk crystals showed significant change at room temperature with $\rho_{pristine}$ equal to 0.64 Ω.m and $\rho_{irradiated}$ equal to 1216 Ω.m showing significant increase of 3-4 orders of magnitude suggesting high density of defects caused by irradiated almost becoming an insulator.

4.3. UV-Vis Spectroscopy

UV-Vis spectroscopy measurements were performed on all the irradiated bulk crystals to better understand the annealing results. This involved shining light through the samples and recording the transmittance (%) of wavelengths ranging from 300 to 1200 nm. Previous reports on GaN irradiation included crystal damage, resulting in a brown coloration to a clear pristine crystal. Apart from the transmutation of Ga to Ge and N to C, the irradiation process also induces damage and produces defects in the GaN lattice. The primary defects generated during irradiation (whether neutron or gamma irradiation) are Frenkel pairs, which consist of a vacancy and an interstitial defect. Examples include nitrogen vacancies, nitrogen interstitials, and Ga vacancies [76]. After the annealing process, most of these defects are eliminated, restoring transparency to the samples. None of our samples showed any discoloration.
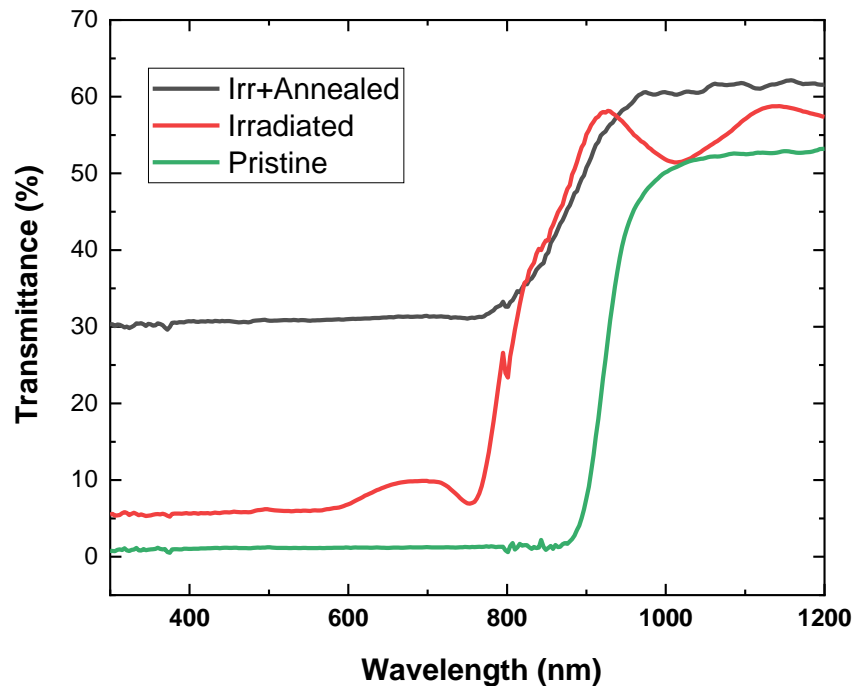
Figure 42: UV-Vis Spectra on Various WSe$_2$ Bulk Crystals.

In figure 42, the green curve represents the UV-Vis spectrum of a WSe_2 crystal before irradiation. The red curve represents the spectrum after the irradiation process, and the black curve represents the spectrum after both irradiation and annealing. In the range of 825 nm to 950 nm, the transmittance drops nearly to 0% from 50% in the pristine sample. The %T drops to zero from 950 to 850 nm means that no light is transmitted through the WSe_2 crystal in this wavelength range, corresponding to the material's absorption edge. The absorption edge is related to the material's band gap, the minimum energy required to excite an electron from the valence band to the conduction band. The band gap of WSe_2 crystal is about 1.3 eV, corresponding to a wavelength of about 950 nm.

Irradiated crystal shows two defect or impurity peaks at 1150 nm (1.1 eV) and 650 nm (1.9 eV) and the transmittance starts dropping from 750 nm to 850 nm, corresponding to a blue shift in the absorption edge of the material. The blue shift means that the band gap of the material increases, which could be due to an increase in strain or disorder in the lattice structure of WSe_2 crystal[85]. The peak at 650 nm indicates another light absorption at this wavelength, possibly due to another defect state or impurity in the band gap of WSe_2 crystal. Post annealing, the defects peaks disappear due to increasing thermal energy to remove the lattice disorder. The blue shift is reduced and bandgap is close to the pristine crystal. The transmission from 300 to 800 nm stays constant at 30% there are still some optical transitions above band gap that can absorb light and reduce transmission. But it does not reduce further because these transitions do not completely absorb all light because some vacancies may be caused by annealing.

Hence Raman and PL measurements at low temperatures were repeated for monolayers exfoliated from annealed crystal at 480 °C for 30 mins with both WSe_2 and WS_2. To consider the annealing effects and be able to differentiate characteristic effects

from neutron irradiation, pristine crystals were also annealed in the same conditions. Monolayers were exfoliated further from these.

4.4. Effects of Annealing

To conserve energy and momentum, atoms can recoil from gamma ray or particle emissions after thermal neutron capture. Fast neutrons ~3% can cause atomic displacements creating vacancies. Based on the theory of transmutation discussed in Chapter 4, some estimates can be made for the rate at which W or In atoms will displace due to recoils from beta and gamma emissions. The number of displaced atoms can be given by

$$\frac{dN}{dt} = N_T \emptyset \sigma \vartheta$$

Where N_T is the number of target atoms per unit volume, $\emptyset$ is the flux of damaging particles, σ is be the abundance and ϑ the number of displacements per incident damaging particle. This gives 10^5 atomic displacements in Tungsten[86]. Hence, thermal annealing was conducted.
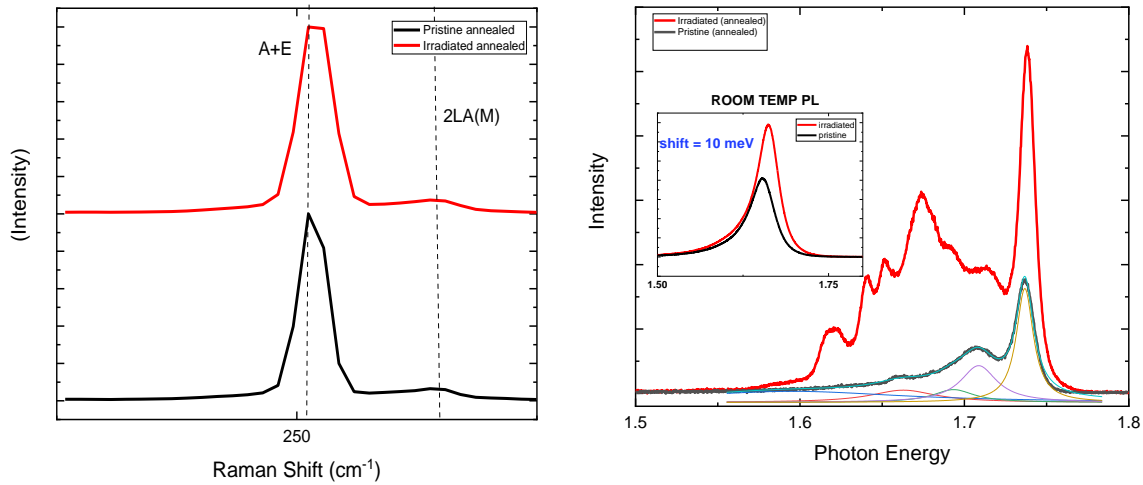
Figure 43: Effects of Annealing on WSe₂ Monolayer: **a** Raman Spectra of Pristine and Irradiated Monolayer **b** PL Spectra at 77 K Inset: Room Temperature PL.

Raman spectroscopy measurements performed on pristine and irradiated crystals were done post annealing. In WSe₂ monolayer, the A+E mode at 251 cm⁻¹ blue shifts by 0.1 cm⁻¹ and shows 0.5 cm⁻¹ increase in FWHM (figure 43 a), indicating the lattice strain and hardening caused by radiation is released.

Other higher frequency Raman modes show slight broadening and no significant change in peak positions. Room temperature PL spectra show an increase in the PL intensity of irradiated monolayer after annealing, and pristine PL spectra are quenched by 30%. The PL intensity of annealed and irradiated monolayer is comparable to the pristine monolayer that is not annealed and blue shifts by 10meV. PL spectra show a significant change in the line widths and peak positions, as evident by new defects related to peaks formed at 1.64 and 1.65 eV, indicating a binding energy of 100 and 90 meV, respectively (table 9). The FWHM of these peaks are 8 meV and 12 meV, respectively. There are no significant changes in neutral exciton and trion energies, but they show a slight reduction in their linewidth as opposed to broadening in the non-annealed samples. The PL spectra for pristine crystals are characterized by selenium vacancies due to annealing and intrinsic

80

bound excitons, as seen in the pristine non-annealed sample. However, dopant states near CBM and Se vacancies characterize the irradiated and annealed monolayer.

Based on first principle calculations, the binding energy of Rhenium dopants in the WSe_2 monolayer is 90-100 meV indicating the n-type doping characteristics nature of Re in WSe_2, which is expected since Re atoms have one more valence electron than W[87]. These defect bands are also expected to split by 0.2-0.3 eV due to spin-orbit coupling[34]. Deep donor states and higher binding energies are expected in 2D TMDCs due to reduced dielectric screening and quantum confinement[87].

Table 9: Photoluminescence of Annealed WSe_2 Monolayers at 77 K.

Pristine annealed		Irradiated Annealed	
Xc (eV)	FWHM (meV)	Xc (eV)	FWHM (meV)
1.6266	48.8	1.619	20.4
n.d.	n.d.	1.640	7.9
n.d.	n.d.	1.651	12.1
1.661	29.1	1.673	27.5
1.688	34.1	1.695	24.5
1.709 (X_T^-)	26.7	1.714 (X_T^-)	21.5
1.737 (X_o)	12.6	1.738 (X_o)	10.1
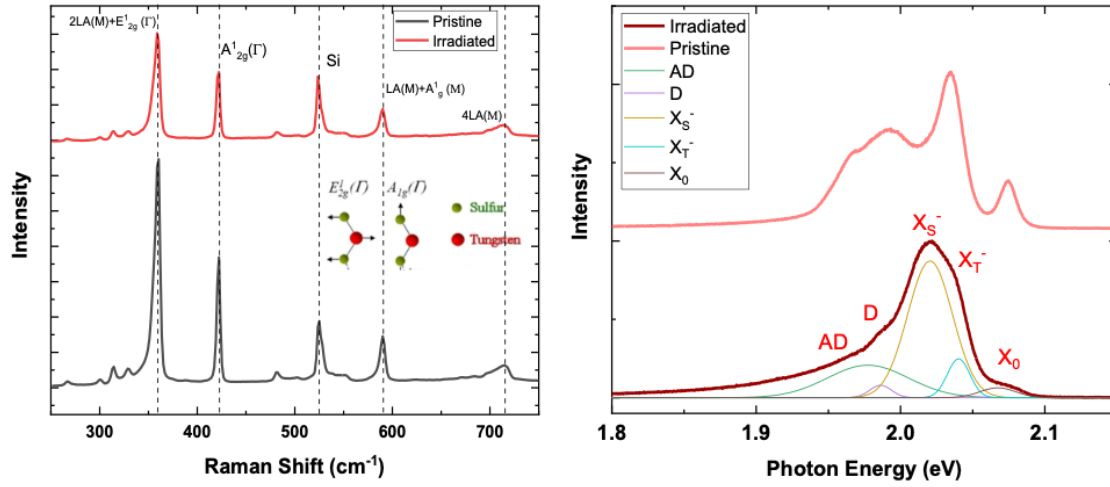
Figure 44: a Raman Spectra of Annealed Pristine and Irradiated WS₂ Monolayers **b** PL Spectra of Annealed Pristine and Irradiated WS₂ Monolayers at 77 K.

Table 10: Raman Spectra Analysis of Annealed WS₂ Monolayers at 77 K.

Pristine annealed		Irradiated annealed	
Xc	FWHM	Xc	FWHM
267.12 ± 0.52	7.67 ± 2.01	267.38 ± 0.18	6.58 ± 0.84
300.36 ± 0.22	3.20 ± 0.56	299.90 ± 0.26	4.82 ± 0.88
313.73 ± 0.08	3.33 ± 0.37	313.69 ± 0.09	4.60 ± 0.34
328.13 ± 0.15	9.30 ± 0.57	327.97 ± 0.14	5.61 ± 0.50
358.29 ± 0.08	6.99 ± 0.32	358.24 ± 0.06	6.62 ± 0.19
421.71± 0.06	3.20 ± 0.18	421.49 ± 0.04	2.70 ± 0.22
527.23 ± 0.36	8.31 ± 1.08	527.26 ± 0.27	6.46 ± 0.86
589.44 ± 0.20	5.48 ± 0.60	589.35 ± 21.10	4.81 ± 0.57
710.20 ± 1.10	17.26 ± 3.70	708.93 ± 1.18	35.11 ± 5.65

Post-annealing Raman spectra of pristine and irradiated monolayer WS₂ show a redshift of 0.3 cm⁻¹ and a reduction in FWHM of 0.5 cm⁻¹ in the A^1_{2g} peak at 421 cm⁻¹. A detailed analysis of all the peaks in figure 44 a is shown in table 10

The most significant change seen in low-temperature PL spectra (figure 44 b) is in singlet trion (X$_S^-$), as shown in table 11. The singlet trion to neutral exciton intensity (area) ratio doubles, followed by a 28 meV reduction in binding energy and 27 meV reduction in

FWHM, indicating an increase in electron density, most likely by Re donors[83]. The new peak (D) at 1.983 eV is only seen in the irradiated monolayer with 100meV binding energy. The FWHM of this peak is ~18 meV is much smaller than previously observed defect peaks in unencapsulated samples.[88,89] PL spectra from several samples were analyzed to confirm this emission, which is most likely a localized emission from Re-defect[90,91]. Previous first-principle calculations and experimental studies report a Re-related defect emission of ~140 meV below the free exciton peak. This high ionization energy is similar to what was seen in Re-WSe$_2$ in the previous section due to quantum confinement and reduced dielectric screening.

Another defect peak seen at 1.961 eV and the neutral exciton peak at 2.08 eV are significantly broadened in the irradiated sample. Further theoretical and experimental studies are required to probe these emissions.

Table 11: PL Spectra Analysis of Annealed WS$_2$ Monolayers at 77 K.

Xc (eV)	FWHM (meV)	Xc (eV)	FWHM (meV)	Change
1.963 (Vs)	20.36	1.961 (Vs)	66.26	No shift 17 meV broadened.
n.d.	n.d.	1.983	17.77	New peak
1.995 (X_S^-)	63.09	2.019 (X_S^-)	36.78	27 meV narrowed, 24 meV blue shift
2.035 (X_T^-)	20.1	2.036 (X_T^-)	18.31	No shift, ~~seven~~ 7 meV narrowed.
2.075(X_o)	4.34	2.077 (X_o)	29	No shift, 23 meV broadened.

4.4.1. Effects of Sulfur-Rich Annealing on WS$_2$ Monolayer

Another set of annealing experiments was conducted on WS$_2$ pristine and irradiated bulk crystals, but this time in a sulfur-rich environment. Elemental Sulfur was

kept at 200 °C upstream, with the crystals at 480 °C. Argon gas was flown during the entire process at 150 sccm. The room temperature PL spectra show a 12 meV redshift with a 20% quenching in the irradiated monolayer (figure 45 a). This significantly improved from previous results of 70% quenching in the room temperature PL spectra without S-rich annealing. This quenching is still attributed to a higher density of trions; however, the scattering due to sulfur vacancies is significantly reduced.
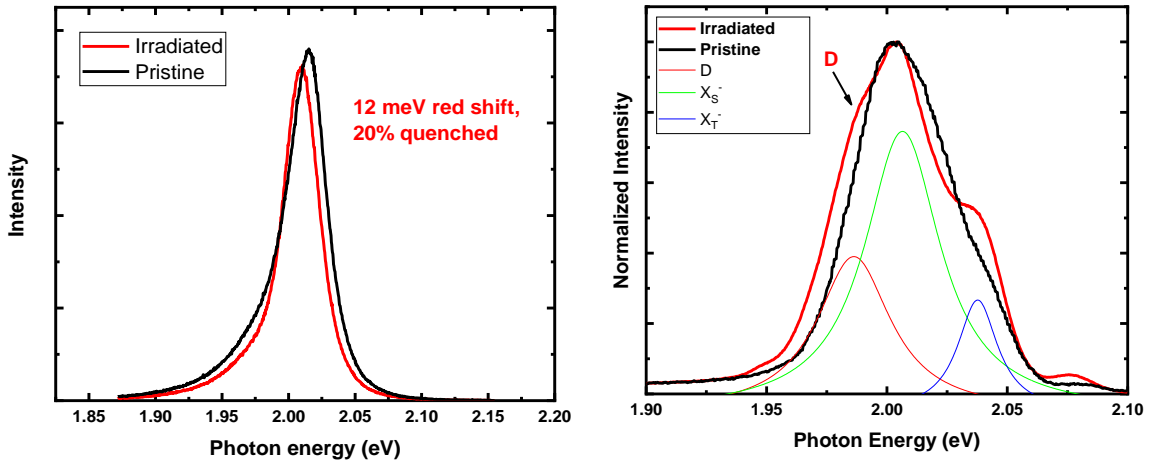
Figure 45: PL Spectra of Pristine and Irradiated WS$_2$ Monolayers Exfoliated from Bulk Crystals Annealed in S-Rich Conditions at **a** Room Temperature and **b**—77 K.

At 77 K, peaks at 1.947 eV and 1.986 eV are more pronounced (table 12) in the irradiated sample. Notably, the peak at 1.987 eV shows a five-fold increase in intensity (area) and its ratio concerning neutral exciton intensity. This indicates that the density of defects at that energy state is much higher than before. Similarly, the singlet trion to neutral exciton ratio has increased by 70%, whereas the triplet trion to neutral exciton ratio has increased by 100%; this shows an increased density of electrons. Notably, the relative abundance of trions, i.e., the ratio of singlet trion to triplet trion, did not change after irradiation. The intensity of subgap peaks after minimizing the formation of sulfur vacancies has increased significantly. These peaks are still broad compared to linewidths

seen in WSe$_2$ monolayers, indicating that 480 ^{o}C annealing temperature might be higher

for WS$_2$. Hence, a lower temperature high enough to release the strain caused by lattice

dislocations is needed.

Table 12: PL Spectra Analysis of Annealed WS$_2$ Monolayers from S-Rich Conditions
at 77 K.

Pristine			Irradiated		
Xc (eV)	FWHM (meV)	I(X)/I(Xo)	Xc (cm^{-1})	FWHM (meV)	I(X)/I(Xo)
-	-	-	1.947	9.76	0.24±0.01
1.986	17.67	3.38 ± 0.8	1.986	24.34	18.46 ±1.2
1.997	31.98	15.5± 3.3	-	-	-
2.016	32.32	22.8 ± 4.5	2.005	33.69	38.75±1.38
2.038	19.71	8.8 ± 4.6	2.037	17.07	16.09±1.02
2.079	24.13	1	2.078	15.65	1

5. CONCLUSIONS AND OUTLOOK

Reliable and scalable metallic doping (p-type or n-type) in 2D materials is challenging due to high dopant formation energies and increased creation of unwanted defects from conventional methods. Neutron Transmutation Doping provides reliable, precise, and controllable doping in bulk crystals. This work mentions that the doping effects can be conveniently extended to a few layers or monolayers. Monolayers exfoliated from several spots and depths of the bulk crystal show similar properties indicating relatively uniform doping. This could be achieved due to proper tuning of the reactor's thermal neutron flux and optimum sample geometries.

Another challenge for doping is reliability and faster quantification of doping concentration. The gamma spectroscopy framework mentioned in this work is a highly sensitive characterization technique to quantify trace-level dopants in the crystal. Once this framework is established, detecting highly precise dopants will be relatively more straightforward. The only condition is that a significant amount of starting material is required for accurate analysis since higher masses will cause higher disintegrations. In this work, the results from Gamma spectroscopy were confirmed by Secondary Ion Mass Spectrometry (SIMS) (0.006%) which showed a slightly higher concentration of Rhenium dopants (0.004%) in WSe_2. Tin dopants in Indium Selenide could not be directly identified from Gamma due to faster decaying isotopes of Indium. It could not be detected using SIMS either due to the most significant number of stable Sn isotopes (around ten), increasing the dilution factor and error in detection.

For this work, a very low neutron flux was chosen due to safety protocols and limited ability to work with radioactive materials in a university setting. Irradiation time

86

was calculated based on the higher limit of exempt radioactivity and set to 1 hour. This enabled safer transfer, storage, and handling of these beta emitter materials. A low doping concentration, in the range of 0.01%, was achieved in this process. Consequently, meager differences were observed after rigorous pristine and irradiated monolayer analysis.

It was found that despite low doping levels, atomic dislocations caused due to recoil caused by Gamma and Beta emissions. This resulted in radiation-induced defects, as shown in the UV-Vis spectra. However, post-thermal annealing treatment, some of these effects became pronounced. New defect-related emissions were observed in monolayer WSe_2 and WS_2 at liquid nitrogen emissions, which are not observed in pristine samples. These defect-related emissions had a narrow linewidth of 8meV and 18-meV from WSe_2 and WS_2, respectively, much lower than non-encapsulated defect-related emissions in these materials. An overall increase in the density of trions and reduction in their binding energies were observed, which is likely an effect of increased electron density attributing to Re donor states.

NTD is a precise and reliable doping technique but has significant limitations due to the requirement of a research reactor and the increased radioactivity involved. An average semiconductor industry worker is not trained to handle radioactive materials, which can lead to safety issues. Secondly, some elements can stay radioactive at higher neutron flux for long, hindering their widescale commercialization. In most cases, NTD will cause n-type doping due to beta decay. Hence, p-type doping via NTD will require isotope selection and separation techniques.

The ability to incorporate precise levels of dopants in TMD monolayers depends on the purity of the pristine crystals. Neutron doping can be tuned by controlling neutron flux, irradiation times, sample geometry, and annealing regimes. This high precision and control of dopants lead to exotic spin-valley polarization effects in TMD monolayers,

demanding detailed studies like STEM and STM on the nature of defects post neutron irradiation and thermal annealing step. It is seen that annealing improves crystallinity and restores electrical conductivity, as shown by Four-probe measurements. However, it also increases the concentrations of Se or S vacancies. Hence, Se-rich or S-rich annealing conditions can improve the defect-related emissions by increasing the radiative recombination.

Rhenium dopants in monolayer WSe_2 and WS_2 have very high ionization energies, as shown in this work and previous works. Implementing external dopant activation techniques like thermal and laser annealing will be helpful for dopant ionizations. Recently, it was shown that hBN encapsulation helps reduce excitonic linewidths, and high-k dielectric encapsulation can increase dielectric screening reducing the binding energy of the dopants. Localized point defects also cause single photon emissions at lower temperatures in TMD monolayers, useful in quantum information applications and cryptography.

REFERENCES

1   Burbidge, E. M., Burbidge, G. R., Fowler, W. A. & Hoyle, F. Synthesis of the Elements in Stars. *Reviews of Modern Physics* **29**, 547-650, doi:10.1103/RevModPhys.29.547 (1957).

2   Bromm, V. Formation of the first stars. *Reports on Progress in Physics* **76**, 112901 (2013).

3   Cowan, J. J. *et al.* Origin of the heaviest elements: The rapid neutron-capture process. *Reviews of Modern Physics* **93**, 015002 (2021).

4   Ferrari, A. C. *et al.* Raman spectrum of graphene and graphene layers. *Physical review letters* **97**, 187401 (2006).

5   Inagaki, M., Kang, F., Toyoda, M. & Konno, H. in *Advanced Materials Science and Engineering of Carbon*   (eds Michio Inagaki, Feiyu Kang, Masahiro Toyoda, & Hidetaka Konno) 1-13 (Butterworth-Heinemann, 2014).

6   Gan, Z. X. *et al.* Quantum confinement effects across two-dimensional planes in MoS_2 quantum dots. *Applied Physics Letters* **106**, doi:10.1063/1.4922551 (2015).

7   Stanford, M. G., Rack, P. D. & Jariwala, D. Emerging nanofabrication and quantum confinement techniques for 2D materials beyond graphene. *npj 2D Materials and Applications* **2**, 20 (2018).

8   Kumar, A. & Ahluwalia, P. K. Electronic structure of transition metal dichalcogenides monolayers 1H-MX2 (M = Mo, W; X = S, Se, Te) from ab-initio theory: new direct band gap semiconductors. *The European Physical Journal B* **85**, 186, doi:10.1140/epjb/e2012-30070-x (2012).

9   He, K. *et al.* Tightly bound excitons in monolayer WSe 2. *Physical review letters* **113**, 026803 (2014).

10 Chernikov, A. *et al.* Exciton Binding Energy and Nonhydrogenic Rydberg Series in Monolayer WS2. *Physical Review Letters* **113**, 076802, doi:10.1103/PhysRevLett.113.076802 (2014).

11 Ross, J. S. *et al.* Electrical control of neutral and charged excitons in a monolayer semiconductor. *Nature communications* **4**, 1474 (2013).

12 Berkelbach, T. C., Hybertsen, M. S. & Reichman, D. R. Theory of neutral and charged excitons in monolayer transition metal dichalcogenides. *Physical Review B* **88**, 045318 (2013).

13 You, Y. *et al.* Observation of biexcitons in monolayer WSe 2. *Nature Physics* **11**, 477-481 (2015).

14 Mak, K. F., Lee, C., Hone, J., Shan, J. & Heinz, T. F. Atomically thin MoS_2: a new direct-gap semiconductor. *Physical review letters* **105**, 136805 (2010).

15 Splendiani, A. *et al.* Emerging photoluminescence in monolayer MoS_2. *Nano letters* **10**, 1271-1275 (2010).

16   Cappelluti, E., Roldán, R., Silva-Guillén, J. A., Ordejón, P. & Guinea, F. Tight-binding model and direct-gap/indirect-gap transition in single-layer and multilayer MoS_2. *Physical Review B* **88**, 075409, doi:10.1103/PhysRevB.88.075409 (2013).

17   Kormányos, A. *et al.* k· p theory for two-dimensional transition metal dichalcogenide semiconductors. *2D Materials* **2**, 022001 (2015).

18   Moody, G. *et al.* Intrinsic homogeneous linewidth and broadening mechanisms of excitons in monolayer transition metal dichalcogenides. *Nature communications* **6**, 8315 (2015).

19   Ajayi, O. A. *et al.* Approaching the intrinsic photoluminescence linewidth in transition metal dichalcogenide monolayers. *2D Materials* **4**, 031011 (2017).

20   Selig, M. *et al.* Excitonic linewidth and coherence lifetime in monolayer transition metal dichalcogenides. *Nature communications* **7**, 13279 (2016).

21   Selig, M. *et al.* Dark and bright exciton formation, thermalization, and photoluminescence in monolayer transition metal dichalcogenides. *2D Materials* **5**, 035017 (2018).

22   Sun, D. *et al.* Observation of rapid exciton–exciton annihilation in monolayer molybdenum disulfide. *Nano letters* **14**, 5625-5629 (2014).

23   Cadiz, F. *et al.* Excitonic linewidth approaching the homogeneous limit in MoS 2-based van der Waals heterostructures. *Physical Review X* **7**, 021026 (2017).

24   Castelletto, S. *et al.* Color centers enabled by direct femto-second laser writing in wide bandgap semiconductors. *Nanomaterials* **11**, 72 (2020).

25   Gutierrez, J. *et al.* Scanning Hall probe microscopy of unconventional vortex patterns in the two-gap MgB 2 superconductor. *Physical Review B* **85**, 094511 (2012).

26   Chen, Y.-H. *et al.* Bandgap control in two-dimensional semiconductors via coherent doping of plasmonic hot electrons. *Nature Communications* **12**, 4332 (2021).

27   Liang, Q., Zhang, Q., Zhao, X., Liu, M. & Wee, A. T. S. Defect Engineering of Two-Dimensional Transition-Metal Dichalcogenides: Applications, Challenges, and Opportunities. *ACS Nano* **15**, 2165-2181, doi:10.1021/acsnano.0c09666 (2021).

28   Yang, X., Guo, S., Chan, F., Wong, K. & Ching, W. Analytic solution of a two-dimensional hydrogen atom. I. Nonrelativistic theory. *Physical Review A* **43**, 1186 (1991).

29   Tongay, S. *et al.* Defects activated photoluminescence in two-dimensional semiconductors: interplay between bound, charged and free excitons. *Scientific Reports* **3**, 2657, doi:10.1038/srep02657 (2013).

30   Mouri, S., Miyauchi, Y. & Matsuda, K. Tunable photoluminescence of monolayer MoS_2 via chemical doping. *Nano letters* **13**, 5944-5948 (2013).

31   Xu, H., Fathipour, S., Kinder, E. W., Seabaugh, A. C. & Fullerton-Shirey, S. K. Reconfigurable ion gating of 2H-MoTe2 field-effect transistors using poly (ethylene oxide)-CsClO4 solid polymer electrolyte. *ACS nano* **9**, 4900-4910 (2015).

32   Zhang, K. *et al.* Manganese doping of monolayer MoS_2: the substrate is critical. *Nano letters* **15**, 6586-6591 (2015).

33   Zhao, P. *et al.* Air stable p-doping of WSe2 by covalent functionalization. *ACS nano* **8**, 10808-10814 (2014).

34   Kozhakhmetov, A. *et al.* Scalable Substitutional Re-Doping and its Impact on the Optical and Electronic Properties of Tungsten Diselenide. *Advanced Materials* **32**, 2005159, doi:https://doi.org/10.1002/adma.202005159 (2020).

35   Addou, R. & Colombo, L. *Defects in Two-Dimensional Materials*. (Elsevier, 2022).

36   Han, D. *et al.* Chemical Trend of Transition-Metal Doping in WSe2. *Physical Review Applied* **12**, 034038, doi:10.1103/PhysRevApplied.12.034038 (2019).

37   Wildervanck, J. C. & Jellinek, F. The dichalcogenides of technetium and rhenium. *Journal of the Less Common Metals* **24**, 73-81, doi:https://doi.org/10.1016/0022-5088(71)90168-8 (1971).

38   O'brien, J. L., Furusawa, A. & Vučković, J. Photonic quantum technologies. *Nature Photonics* **3**, 687-695 (2009).

39   Aharonovich, I., Englund, D. & Toth, M. Solid-state single-photon emitters. *Nature photonics* **10**, 631-641 (2016).

40   He, Y.-M. *et al.* Single quantum emitters in monolayer semiconductors. *Nature nanotechnology* **10**, 497-502 (2015).

41   Linhart, L. *et al.* Localized intervalley defect excitons as single-photon emitters in WSe 2. *Physical review letters* **123**, 146401 (2019).

42   Mitterreiter, E. *et al.* The role of chalcogen vacancies for atomic defect emission in MoS_2. *Nature communications* **12**, 3822 (2021).

43   Parto, K., Azzam, S. I., Banerjee, K. & Moody, G. Defect and strain engineering of monolayer WSe2 enables site-controlled single-photon emission up to 150 K. *Nature Communications* **12**, 3585, doi:10.1038/s41467-021-23709-5 (2021).

44   Utama, M. I. B. *et al.* Chemomechanical modification of quantum emission in monolayer WSe2. *Nature communications* **14**, 2193 (2023).

45   Kim, K. S. *et al.* Non-epitaxial single-crystal 2D material growth by geometric confinement. *Nature* **614**, 88-94, doi:10.1038/s41586-022-05524-0 (2023).

46   Peer, S., Michael, B., Robert, G. & Marcus, S. in *Advanced Topics on Crystal Growth* (ed Ferreira Sukarno Olavo) Ch. 9 (IntechOpen, 2013).

47   Binnewies, M., Glaum, R., Schmidt, M. & Schmidt, P. *Chemical vapor transport reactions*. (Walter de Gruyter, 2012).

48   Schmidt, P., Binnewies, M., Glaum, R. & Schmidt, M. P.

49   Lenz, M. & Gruehn, R. Developments in measuring and calculating chemical vapor transport phenomena demonstrated on Cr, Mo, W, and their compounds. *Chemical reviews* **97**, 2967-2994 (1997).

50   Upadhyayula, L., Loferski, J., Wold, A., Giriat, W. & Kershaw, R. Semiconducting properties of single crystals of n-and p-type tungsten diselenide (WSe2). *Journal of Applied Physics* **39**, 4736-4740 (1968).

51 Legma, J., Vacquier, G. & Casalot, A. Chemical vapour transport of molybdenum and tungsten diselenides by various transport agents. *Journal of crystal growth* **130**, 253-258 (1993).

52 Tripathi, L. N. & Barua, S. Growth and characterization of two-dimensional crystals for communication and energy applications. *Progress in Crystal Growth and Characterization of Materials* **65**, 100465, doi:https://doi.org/10.1016/j.pcrysgrow.2019.100465 (2019).

53 Krug, J. Four lectures on the physics of crystal growth. *Physica A: Statistical Mechanics and its Applications* **313**, 47-82 (2002).

54 May, A. F., Yan, J. & McGuire, M. A. A practical guide for crystal growth of van der Waals layered materials. *Journal of Applied Physics* **128** (2020).

55 Yu, M. L. Chemical enhancement effects in SIMS analysis. *Nuclear Instruments and Methods in Physics Research Section B: Beam Interactions with Materials and Atoms* **15**, 151-158, doi:https://doi.org/10.1016/0168-583X(86)90273-9 (1986).

56 Lyon, L. A. *et al.* Raman spectroscopy. *Analytical Chemistry* **70**, 341-362 (1998).

57 Schroder, D. K. *Semiconductor material and device characterization*. (John Wiley & Sons, 2015).

58 Deutsch, Z., Schwartz, O., Tenne, R., Popovitz-Biro, R. & Oron, D. Two-color antibunching from band-gap engineered colloidal semiconductor nanocrystals. *Nano letters* **12**, 2948-2952 (2012).

59 Chhowalla, M. *et al.* The chemistry of two-dimensional layered transition metal dichalcogenide nanosheets. *Nature chemistry* **5**, 263-275 (2013).

60 Omidi, M. *et al.* in *Biomaterials for Oral and Dental Tissue Engineering*   (eds Lobat Tayebi & Keyvan Moharamzadeh) 97-115 (Woodhead Publishing, 2017).

61 Burany, S. *Scanning Electron Microscopy and X-Ray Microanalysis. .* Vol. 9 (Kluwer Academic, Plenum Publishers, 2003).

62 Goldstein, J. *et al. Scanning Electron Microscopy and X-ray Microanalysis* Vol. XIX (2003).

63 Diffey, B. L. Sources and measurement of ultraviolet radiation. *Methods* **28**, 4-13, doi:https://doi.org/10.1016/S1046-2023(02)00204-9 (2002).

64 Kónya, J. & Nagy, N. M. *Nuclear and radiochemistry*. (Elsevier, 2018).

65 Mughabghab, S. Thermal neutron capture cross sections resonance integrals and g-factors. (2003).

66 Atomics, G. *TRIGA Nuclear Reactors*, <https://www.ga.com/triga/> (

67 Choppin, G. & Ridberg, Y. Nuclear chemistry. (1984).

68 Soum-Sidikov, G. *et al. Study of collision and gamma-cascade times following neutron-capture processes in cryogenic detectors.* (arXiv preprint, 2023).

69 Essig, R., Sholapurkar, M. & Yu, T.-T. Solar neutrinos as a signal and background in direct-detection experiments searching for sub-GeV dark matter with electron recoils. *Physical Review D* **97**, 095029 (2018).

70 Dewey, S., Whetstone, Z. & Kearfott, K. A numerical method for the calibration of in situ gamma ray spectroscopy systems. *Health physics* **98**, 657-671 (2010).

71 Yuan, X. & Mayanovic, R. A. An Empirical Study on Raman Peak Fitting and Its Application to Raman Quantitative Research. *Applied Spectroscopy* **71**, 2325-2338, doi:10.1177/0003702817721527 (2017).

72 Pan, Y. *et al.* Exciton tuning in monolayer WSe2 via substrate induced electron doping. *Nanoscale Advances* **4**, 5102-5108, doi:10.1039/D2NA00495J (2022).

73 Zhao, W. *et al.* Lattice dynamics in mono- and few-layer sheets of WS2 and WSe2. *Nanoscale* **5**, 9677-9683, doi:10.1039/C3NR03052K (2013).

74 Shi, W. *et al.* Raman and photoluminescence spectra of two-dimensional nanocrystallites of monolayer WS2 and WSe2. *2D Materials* **3**, 025016 (2016).

75 Lu, X., Luo, X., Zhang, J., Quek, S. Y. & Xiong, Q. Lattice vibrations and Raman scattering in two-dimensional layered materials beyond graphene. *Nano Research* **9**, 3559-3597 (2016).

76 Li, J. *et al.* Atypical defect-mediated photoluminescence and resonance raman spectroscopy of monolayer Ws2. *The Journal of Physical Chemistry C* **123**, 3900-3907 (2019).

77 Qian, Q., Zhang, Z. & Chen, K. J. In situ resonant raman spectroscopy to monitor the surface functionalization of MoS_2 and Wse2 for High-K integration: A first-principles study. *Langmuir* **34**, 2882-2889 (2018).

78 Lewandowska, R., Bacewicz, R., Filipowicz, J. & Paszkowicz, W. Raman scattering in α-In2Se3 crystals. *Materials Research Bulletin* **36**, 2577-2583, doi:https://doi.org/10.1016/S0025-5408(01)00746-2 (2001).

79 Balakrishnan, N. *et al.* Quantum confinement and photoresponsivity of β-In2Se3 nanosheets grown by physical vapour transport. *2D Materials* **3**, doi:10.1088/2053-1583/3/2/025030 (2016).

80 Zhang, K. *et al.* Tuning the electronic and photonic properties of monolayer MoS_2 via in situ rhenium substitutional doping. *Advanced Functional Materials* **28**, 1706950 (2018).

81 Isobe, Y., Tanaka, M., Yamanaka, S. & Miyake, M. Chemical vapour deposition of rhenium on graphite. *Journal of the Less Common Metals* **152**, 177-184 (1989).

82 Moody, G. *et al. Microsecond Valley Lifetime of Defect-Bound Excitons in Monolayer WSe2*. Vol. 121 057403 (2018).

83 Robert, C. *et al.* Spin/valley pumping of resident electrons in WSe2 and WS2 monolayers. *Nature Communications* **12**, 5455, doi:10.1038/s41467-021-25747-5 (2021).

84 Feng, R. *et al.* Local modulation of excitons and trions in monolayer WS2 by carbon nanotubes. *Nano Research* **13**, 1982-1987, doi:10.1007/s12274-020-2895-5 (2020).

85 Shi, T., Walker, R. C., Jovanovic, I. & Robinson, J. A. Effects of energetic ion irradiation on WSe2/SiC heterostructures. *Scientific Reports* **7**, 4151, doi:10.1038/s41598-017-04042-8 (2017).

86 Meese, J. *Neutron transmutation doping in semiconductors*. (Springer Science & Business Media, 2012).

87 Yang, J.-H. & Yakobson, B. Dimensionality-suppressed chemical doping in 2D semiconductors: the cases of phosphorene, MoS_2, and ReS2 from first-principles. *arXiv preprint arXiv:1711.05094* (2017).

88 Greben, K., Arora, S., Harats, M. G. & Bolotin, K. I. Intrinsic and extrinsic defect-related excitons in TMDCs. *Nano Letters* **20**, 2544-2550 (2020).

89 Carozo, V. *et al.* Optical identification of sulfur vacancies: Bound excitons at the edges of monolayer tungsten disulfide. *Science advances* **3**, e1602813 (2017).

90 Loh, L. *et al.* Impurity-Induced Emission in Re-Doped WS(2) Monolayers. *Nano Lett* **21**, 5293-5300, doi:10.1021/acs.nanolett.1c01439 (2021).

91 Li, S. *et al.* Tunable Doping of Rhenium and Vanadium into Transition Metal Dichalcogenides for Two-Dimensional Electronics. *Advanced Science* **8**, 2004438, doi:https://doi.org/10.1002/advs.202004438 (2021).